NASA/TP—2012–216483

Risk Assessment and scaling for the SLS LH2 ET

Viatcheslav (Slava) Osipov

Ames Research Center, Moffett Field, California
Halyna Hafiychuk
Ekaterina Ponizovskaya-Devine
Dmitry Luchinsky
Michael Khasin,
Vadim Smelyanskiy

December 2012

NASA STI Program ... in Profile

Since its founding, NASA has been dedicated to the advancement of aeronautics and space science. The NASA scientific and technical information (STI) program plays a key part in helping NASA maintain this important role.

The NASA STI program operates under the auspices of the Agency Chief Information Officer. It collects, organizes, provides for archiving, and disseminates NASA's STI. The NASA STI program provides access to the NASA Aeronautics and Space Database and its public interface, the NASA Technical Reports Server, thus providing one of the largest collections of aeronautical and space science STI in the world. Results are published in both non-NASA channels and by NASA in the NASA STI Report Series, which includes the following report types:

- TECHNICAL PUBLICATION. Reports of completed research or a major significant phase of research that present the results of NASA Programs and include extensive data or theoretical analysis. Includes compilations of significant scientific and technical data and information deemed to be of continuing reference value. NASA counterpart of peer-reviewed formal professional papers but has less stringent limitations on manuscript length and extent of graphic presentations.

- TECHNICAL MEMORANDUM. Scientific and technical findings that are preliminary or of specialized interest, e.g., quick release reports, working papers, and bibliographies that contain minimal annotation. Does not contain extensive analysis.

- CONTRACTOR REPORT. Scientific and technical findings by NASA-sponsored contractors and grantees.

- CONFERENCE PUBLICATION. Collected papers from scientific and technical conferences, symposia, seminars, or other meetings sponsored or co-sponsored by NASA.

- SPECIAL PUBLICATION. Scientific, technical, or historical information from NASA programs, projects, and missions, often concerned with subjects having substantial public interest.

- TECHNICAL TRANSLATION. English-language translations of foreign scientific and technical material pertinent to NASA's mission.

Specialized services also include organizing and publishing research results, distributing specialized research announcements and feeds, providing information desk and personal search support, and enabling data exchange services.

For more information about the NASA STI program, see the following:

- Access the NASA STI program home page at http://www.sti.nasa.gov

- E-mail your question to help@sti.nasa.gov

- Fax your question to the NASA STI Information Desk at 443-757-5803

- Phone the NASA STI Information Desk at 443-757-5802

- Write to:
  STI Information Desk
  NASA Center for AeroSpace Information
  7115 Standard Drive
  Hanover, MD 21076-1320

NASA/TP—2012–216483

Risk Assessment and scaling for the SLS LH2 ET

Viatcheslav (Slava) Osipov

Ames Research Center, Moffett Field, California

Halyna Hafiychuk
Ekaterina Ponizovskaya-Devine
Dmitry Luchinsky
Michael Khasin,
Vadim Smelyanskiy

National Aeronautics and
Space Administration

Ames Research Center
Moffett Field, CA 94035-1000

December 2012

Acknowledgments

Available from:

NASA Center for AeroSpace Information
7115 Standard Drive
Hanover, MD 21076-1320
443-757-5802

ABSTRACT

In this report the main physics processes in LH2 tank during prepress and rocket flight are studied. The goal of this investigation is to analyze possible hazards and to make risk assessment in proposed LH2 tank designs for SLS with 5 engines (the situation with 4 engines is less critical). For analysis we use the multinode model (MNM) developed by us and presented in a separate report and also 3D ANSYS simulations. We carry out simulation and theoretical analysis the physics processes such as (i) accumulation of bubbles in LH2 during replenish stage and their collapsing in the liquid during the prepress; (ii) condensation-evaporation at the liquid-vapor interface and tank wall, (iv) heating the liquid near the interface and wall due to condensation and environment heat, (v) injection of hot He during prepress and of hot GH2 during flight, (vi) mixing and cooling of the injected gases due to heat transfer between the gases, liquid and the tank wall. We analyze the effects of these physical processes on the thermo- and fluid gas dynamics in the ullage and on the stratification of temperature in the liquid and assess the associated hazards. A special emphasize is put on the scaling predictions for the larger SLS LH2 tank.

CONTENT

Nomenclature

ρ	= density
p	= pressure
p_c	= critical pressure for gas
T	= temperature
T_c	= critical temperature for gas
T_s	= surface or interface temperature
u	= velocity
c	= sound velocity
M	= Mach number, M = u/c, M_0 = u/c_0
C_V	= specific heat for the constant volume
C_P	= specific heat for the constant pressure
γ	= ration of specific heats; $\gamma = c_p/c_V$
g	= gravity
R_t	= radius
S_t	= radius of tank
Ssu	= surface of tank cross-section
r	= total surface of tank
L_D	= thermodiffusion length
q_L	= heat of evaporation
h_T	= heat transfer coefficient
j	= mass flow density [$j = u\rho$]
J	= mass flow [$J = u\rho S$]
q	= heat flow density
Q	= heat flow
Q_c	= convection heat flow
Q_R	= radiation heat flow
β_T	= thermal expansion coefficient
δ	= boundary layer thickness
k	= thermal conductivity
v	= kinematic viscosity
μ	= dynamical viscosity
Pr	= Prandtl number, $Pr=\mu C_p/k$
Ra	= Raleigh number
Re_x	= Reynolds number
Gr	= Grashof number
Nu	= Nusselt number

Subscripts:

g	= gas
L	= liquid
env	= environment
t	= tank
w	= tank wall
ull	= ullage
eva	= evaporation
p	=condensation
con	
d	

Abbreviations:

LH2	= Liquid Hydrogen
GH2	= Gaseous Hydrogen
MNM	= Multinode Model
SLS	= Space Launch System
3D	= Three dimensional

Introduction

We study main physical processes in the LH2 tank during the prepress and rocket flight. The goal of this research is to analyze the hazards associated with the functioning of the external cryogenic LH2 tank of the Space Shuttle (Fig.1) during the pre-pressurization process and in the course of the flight and their scalability to the proposed SLS design with 5 engines (the situation with 4 engines is less critical). We use both the protocol, material parameters, and the telemetric data for Shuttle flights [1, 2] to fit an uncertain parameter of the multinode model (MNM), developed in our group with use results of the works [3-5]. After an appropriate rescaling MNM is further applied to study the temperature stratification, the ullage pressure dynamics and the associated risks in the LH2 tank in the framework of the proposed SLS designs.

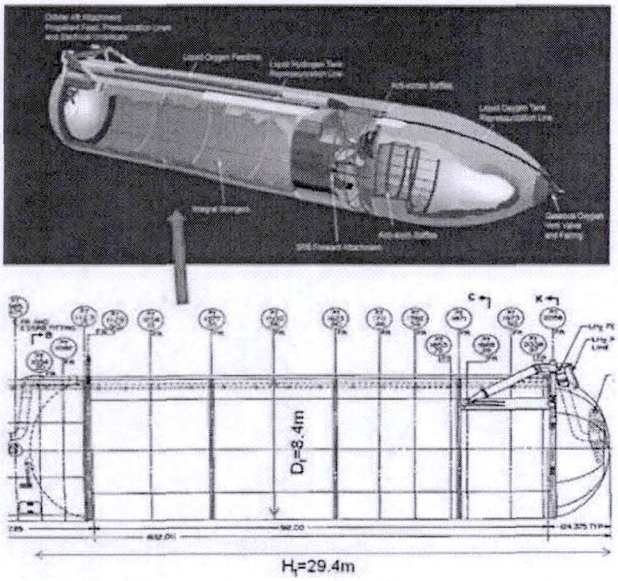

Fig.1. Design of the Shuttle tanks: the shape and parameters of the LH2 tank

1. Boiling near the tank wall and bubbles' collapsing: scaling of the bubbles' volume

LH2 is characterized by a low temperature of boiling [6-8]. Therefore, a very weak heating of the liquid boundary layer near the tank wall by the environment heat flow $Q_{env} = q_{env} S_{sur}$ leads to boiling LH2 (Fig.1-1) by creating bubbles. We show below that the total volume of the bubbles is proportional to the tank height squared H_t^2 due to increase both of the power Q_{env} and the rising time of the bubbles.

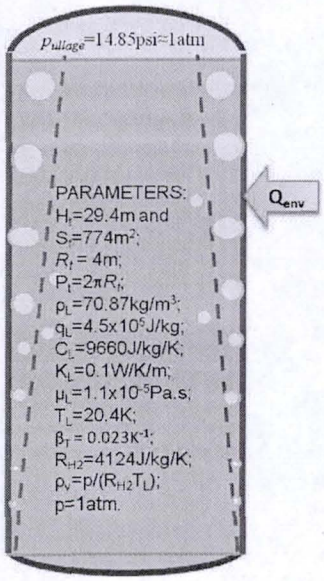

Fig.1-1. Boiling near the LH2 tank wall due to the environmental heat flux.

1.1. Nucleate boiling of liquid in the boundary layer near the wall

During the replenish stage bubbles are generated near the tank wall due to the heat flux q_{env} from the hot environment. The bubbles mass generation rate can be assessed as

$$\dot{m}_{bubble}=\frac{q_{cr..}S_{sur}}{q_L},\ \dot{m}_{bubble}\approx 0.35kg/\sec\ \text{at}\ q_{env}=200w/m^2 \tag{1}$$

The velocity of bubbles rising under the buoyancy force is given by

$$\begin{aligned}&\rho_{vapor}V_{bub}\frac{dv_{bub}}{dt}=gV_{bub}\left(\rho_L-\rho_{vapor}\right)-\frac{C_d}{2}\rho_L v_{bub}^2 S_{bub},\\ &v_{bub}^{stat}\approx\sqrt{\frac{8g\,r_{bub}}{3C_d}},\quad\Rightarrow v_{bub}^{stat}\approx\left(0.4\div 1.8\right)\frac{m}{s},\left(0.04<C_d\le 0.4\right)\end{aligned} \tag{2}$$

Here we estimated the typical size of the bubble is by the LH2 capillary radius $r_{capill}=\sqrt{2\sigma_{LH2}/g\rho_L}=2mm\ \ (\sigma_{LH2}=1.7\cdot 10^{-3}N/m)$. The bubbles number density along the tank wall can be approximated using

$$\frac{d\rho_{bubble}}{dt}=\frac{d\rho_{bubble}}{dx}v_{bub}^{stat}=\frac{q_w S_{sur}}{q_L}\Rightarrow\rho_{bubble}(x)=\frac{q_w S_{sur}}{q_L v_{bubble}^{stat}}x \tag{3}$$

Eq. (3) implies

$$V_{bubble}=\int_0^{H_t}\frac{\rho_{bubble}(x)}{\rho_{bubble,0}}dx=V_{bubble}^0\left(\frac{H_t}{H_{t0}}\right)^2 \tag{4}$$

It follows that the bubble volume is a quadratic function of the tank height length H_t.

1.2. Collapsing of the bubbles during the prepress

During the initial stage of the prepress bubbles will collapse due to increase of the pressure from 1 amt to 3.2atm over ~16 sec. The characteristic time-scale of the collapsing can be estimate from the energy balance

$$4\pi r_{bub}^2 K_L \frac{(T_{sb}-T_L)}{r_{bub}} Nu_{/r_b} \cdot t_{collaps} = V_{bub}\rho_{s,vapor} q_L,$$

where $\rho_{s,vapor}$ is density of saturated H2 vapor at p=3atm and (5)

$$\text{Nusselt number } Nu_{/r_{b0}} = 0.332\left(\frac{\rho_L v_{bubble}^{stat} r_{bubble,0}}{\mu_L}\right)^{1/2}\left(\frac{C_L\mu_L}{K_L}\right)^{1/3} \approx 50,$$

The bubble surface temperature is determined by the ullage pressure [9]

$$T_s(p) = T_c\left(\frac{p}{p_c}\right)^{1/5.3}, T_s = 25K \; at \; p = 3.2atm \tag{6}$$

We find from Eq. (5)

$$t_{collapse} = \frac{\rho_{vapor} q_L r_{bubble,0}^2}{3K_L(T_{sb}-T_L)Nu_{/r_{b0}}}, t_{collapse} < 1\sec \; at \; p > 1.5atm \tag{7}$$

Thus, the bubbles will collapse completely during of the initial stage of the He injection, leading to increase of the ullage volume. The ullage and bubble volumes in Space Shuttle are V_{bubble}=58.25ft^3 and V_{ullage}=372 ft^3 (see Table1), i.e. V_{bubble} / V_{ullage} =16%. While, in SLS LH2 tank with 5 engines V_{bubble}=162.25ft^3 and V_{ullage}=620 ft^3, i.e. V_{bubble} / V_{ullage} =26%. This effect has to be taken into account in the simulation of LH2 tank and in particular of the prepress regime.

2. Main processes of heat transfer in the LH2 tank

The general heat balance in the ullage LH2 tank (Fig. 2-1) can be written as

$$Q_{inject} + Q_{env} = Q_{ullage} + Q_{wall} + Q_L. \tag{8}$$

Here $Q_{inject} + Q_{env}$ is the total heat added to the ullage tank as a result of hot gas injection from the diffuser and the interaction with environment. This heat is spent on heating the gas inthe ullage,

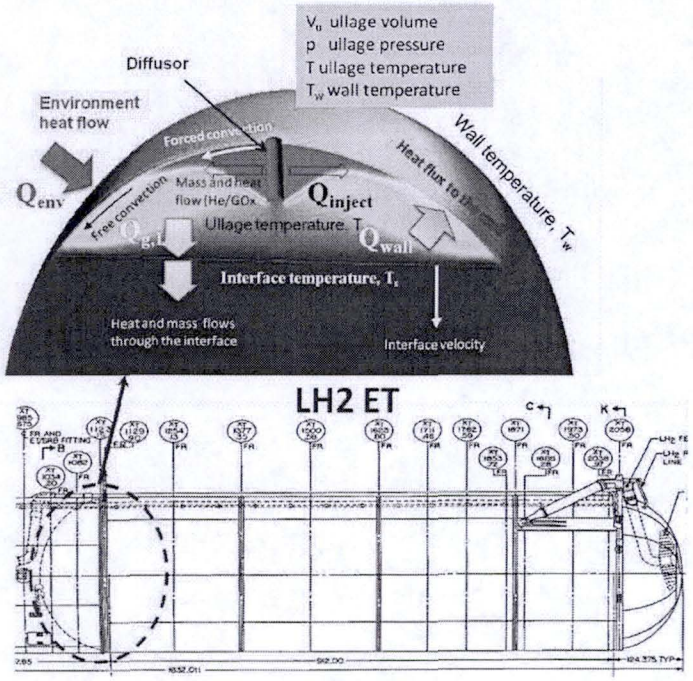

Fig.2-1. LH2 tank design. Main physical processes and variables

Q_{ullage}, heating the tank wall, Q_{wall}, and on condensation-evaporation processes including heating of the surface layer of the liquid , Q_L. The heat flows associated with these processes are sketched in Fig. 2-1, which also defines the variables of the physical model.

We now proceed to analyzing these pathways and estimating their relative importance for the problem of temperature stratification and pressure dynamics in the ullage.

2.1. Condensation-evaporation at the liquid-vapor interface

A possible risk associated with the condensation-evaporation processes at the liquid-gas interface is a deviation of the ullage pressure from its permissible bounds (Fig.1). Here we analyze the evaporation of LH2 due to the hot He or GH2 injection from the diffuser. We notice that the change of the ullage pressure is slow (~sec) compared to the timescale of thermalization of the liquid-vapor interface (< 0.1msec). As a consequence, the quasi-equilibrium near the interface is established for all times with the surface temperature T_s determined by the vapor pressure $p_{vapour} = p_{GH2}$ [9] :

$$T_s = T_c \left(\frac{p_{GOx}}{p_c} \right)^{1/\lambda}, \quad p_s(T) = p_c \left(\frac{T}{T_c} \right)^{\lambda}. \tag{9}$$

Here T_c =33.2K and p_c =13.2atm are the critical temperature and pressure of hydrogen, p_s is the pressure of saturated vapour near the interface and λ=5.3 for H2 (see Fig. 2-2) [6-8].

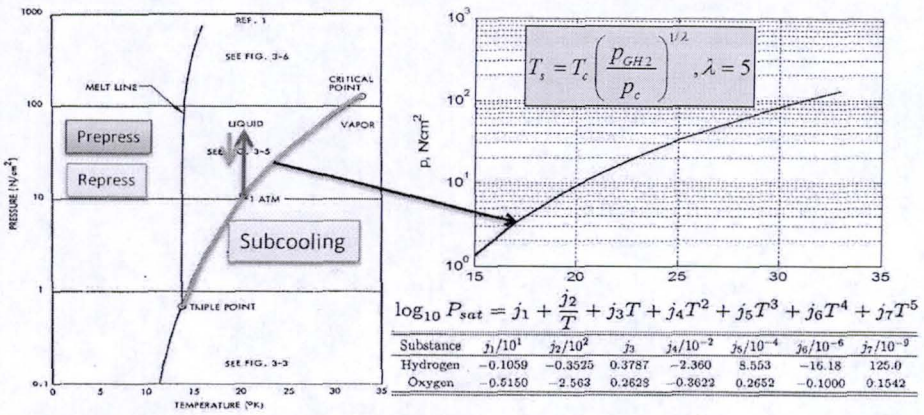

Substance	$j_1/10^1$	$j_2/10^2$	j_3	$j_4/10^{-2}$	$j_5/10^{-4}$	$j_6/10^{-6}$	$j_7/10^{-9}$
Hydrogen	−0.1059	−0.3525	0.3787	−2.360	8.553	−16.18	125.0
Oxygen	−0.5150	−2.563	0.2628	−0.3622	0.2652	−0.1000	0.1542

Fig.2-2 Dependence of saturated vapor pressure on the surface temperature of LH2

Note, that p_s=*1atm* at T_s=T_L=*20.4K*. The partial H2 vapor pressure is p_{GH2}≈*3.2atm=47psi* and p_{GH2}≈*2.25atm=32psi* during the prepress and flight, respectively. For such pressures the liquid surface temperature $T_s > T_L$. Since $T_s > T_L$ and $T_g > T_s$ the convection of both liquid and vapor is absent. (Moreover, our 3D simulations have also shown that the convection induced by the hot gas injection from the diffuser and natural convection near the wall is relatively small near the gas-liquid interface.) Thus, the heat balance in condensation-evaporation processes is established mainly by means of thermo-diffusion at the given surface temperature $T_s(p_{GH2})$. The thermodiffusion is driven by the equation

$$C_{L,g}\rho_{L,g}\frac{\partial T}{\partial t} = \kappa_{L,g}\frac{\partial^2 T}{\partial t^2}, \quad T(0,t) = T_s = const, T(r,\infty) = T_{L0} \tag{10}$$

The solution of is

$$C_{L,g}\rho_{L,g}\frac{\partial T}{\partial t} = \kappa_{L,g}\frac{\partial^2 T}{\partial t^2}, \quad T(0,t) = T_s = const, T(r,\infty) = T_{L0}$$

$$T(r,t) = T_{L0} + (T_s - T_{L0})\,erf\left(\sqrt{\frac{C_L\rho_L x^2}{4\kappa_L t}}\right)$$

Here $\rho_{L,g}, C_{L,g}, \kappa_{L,g}$ are the density, heat capacity, and thermo-conductivity of liquid (gas-vapor); x=0 is the liquid-vapor interface, erf is the error function. Using Eq. **Error! Reference source not found.** we find that the heat flux from the heated surface to the interface

$$\dot{q}_L(x,t) = -\kappa_L\left.\frac{\partial T(x,t)}{\partial x}\right|_{x=0} = \sqrt{\frac{C_L\rho_L\kappa_L(T_s - T_L)^2}{\pi t}} = \left(\sqrt{\frac{4}{\pi}}\right)\kappa_L\frac{T_s - T_L}{L_{DL}}, \tag{11}$$

$$where\ L_{DL} = \sqrt{\frac{\pi\kappa_L t}{C_L\rho_L}}\ \text{is thermodiffusion lenght and}\ \dot{Q}_L = S_L\dot{q}_L.$$

This makes it possible to estimate the condensation mass flow j_{cond} from the following balance equation:

$$\dot{Q}_{cond} = j_{cond}(t)S_L\left(q_L + C_{GH2}(T_g - T_s)\right) = \dot{Q}_L - \dot{Q}_g = S_L\left(\sqrt{\frac{T_s - T_L}{L_{DL}(t)}} - K_g\frac{T_g - T_s}{L_{Dg}(t)}\right), \tag{12}$$

$$j_{cond}(t) = \frac{\sqrt{K_L C_L\rho_L}(T_s - T_L) - \sqrt{K_{GH2}C_{GH2}\rho_{GH2}}(T_g - T_s)}{q_L + C_{GH2}(T_g - T_s)}$$

Here the first term in the left part of Eq. (12) describes the condensation heat flow rate and the second describes the evaporation flow rate. The mass of condensed vapor is given by (11)

$$M_{cond}(t) = \int_0^t S_L(t) j_{cond}(t) dt \tag{13}$$

According to Eq. (12) condensation will be dominant whenever

$$\left(T_g - T_s(p_{GOx})\right) < \left(T_s(p_{GOx}) - T_L\right) \sqrt{\frac{K_L C_L \rho_L}{K_{GOx} C_{GOx} \rho_{GOx}}}, \; T_s(p_{GOx}) = T_c \left(\frac{p_{GOx}}{p_c}\right)^{1/5.3} \tag{14}$$

According to the condition (14), the condensation is dominant when the gas temperature near the liquid-vapor interface T_g < 70K during the prepress when p≈3.2 atm and T_g < 65K during the flight when p≈2.25atm. For the estimation of the thermo-diffusion length in the gas we used characteristics of pure H2 prevalent in the vicinity of the interface. This result agrees with the experimental data [10] presented in Fig. 2-4. The point in Fig. 2-4, right correspond of our estimation for p=32psi.

MNM simulation showed that the effective temperature of the ullage gas near the interface is less than 70K. Therefore, the condensation is dominant in the LH2 tank during the prepress (Fig.2-5) when the partial GH2 pressure is higher than 2atm (Fig.2-6). However, it is expected (see estimation in Fig. 2-4, left) that the condensation mass flux is relatively small in comparison with rates of injection of both hot He (j_{He}=0.6kg/sec) and H2 (j_{H2}=0.47kg/sec) from the tank diffuser. We note that the condensation rate found in MNM simulation is an overestimate since a higher averaged temperature in a relatively wide layer is used to calculate the rate.

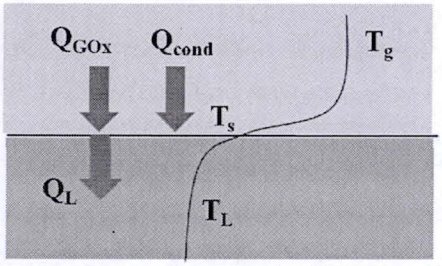

Fig.2-3: Temperature profile near the liquid-gas interface

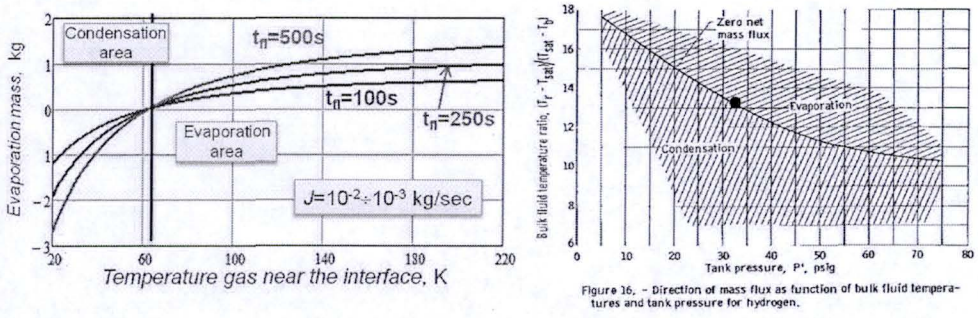

Fig. 2-4 Evaporated mass (left) and critical temperature (right) as function of vapor He pressure: theoretical estimations (left at p_{GH2}=2.25atm) and experimental data [9]

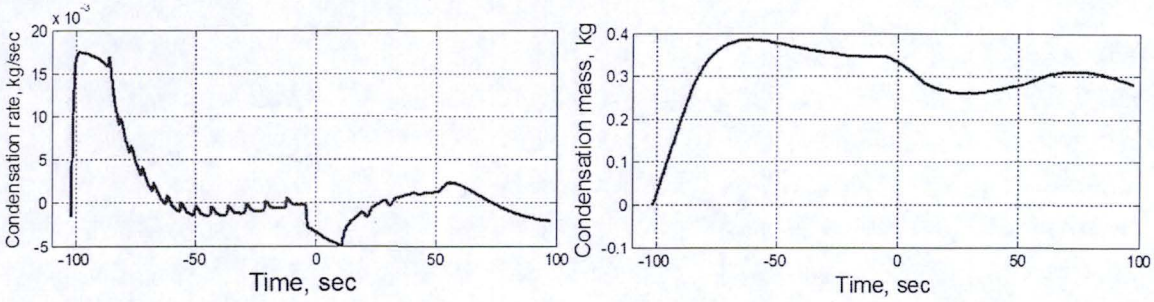

Fig. 2-5. Time-traces of the condensation flow rate (left) and the condensed mass (right). Results of the MNM simulation.

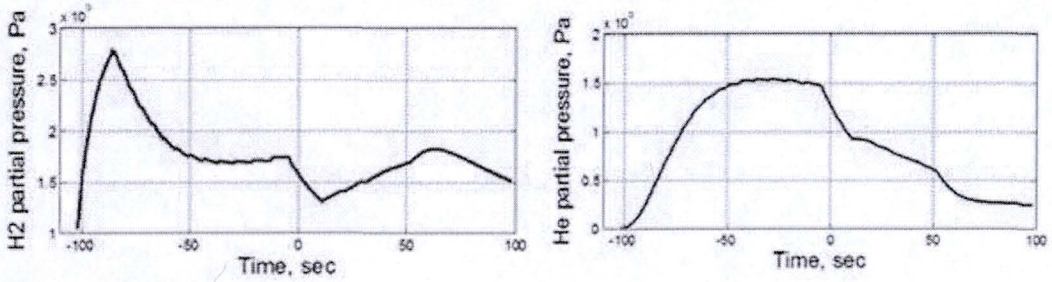

Fig. 2-6. Partial pressures of H2 vapor and He near the liquid-vapor interface. Results of the MNM simulation.

2.2. Cooling of the ullage gas by condensation at the interface

The heat flux into the liquid associated with the condensation is given by

$$\dot{Q}_{gL} \equiv \frac{dQ_{gL}}{dt} = \kappa_g \frac{(T_g - T_s)}{L_{Dg}(t)} S_L(t) = (T_g - T_s) S_L(t) \sqrt{\frac{\kappa_g C_g \rho_g}{\pi t}},$$

$$L_{Dg} = \sqrt{\frac{\pi \kappa_g t}{C_g \rho_g}} \text{ is thermodiffusion lenght in the gas} \qquad (15)$$

The total heat due to the condensation of GH2 can be estimated as

$$Q_{gL}(t) \approx (T_g - T_s) \overline{S}_L \sqrt{\kappa_L C_L \rho_L (4t/\pi)},$$

$$Q_{gL}(t_{\text{prepress}}) \approx 4.6 \times 10^5 J \text{ and } Q_{gL}(t_{\text{flight}}) \approx 10^6 J \qquad (16)$$

The heat of injected He during of the prepress (t≈100sec) and the total heat of injected hot GH2 during the flight (t_{flight} =500sec) are estimated as follows

$$Q_{inject}^{He} = C_{p,He} T_{He} J_{He} t_{prepres} = 8.7 \cdot 10^7 J, \; Q_{inject}^{GH2} = C_{p,GH2} T_{GH2} J_{GH2} t_{flight} = 9.1 \cdot 10^8 J. \qquad (17)$$

Thus, the condensation weakly affects the general ullage heat balance: $Q_{gL}(t_{flight})/Q_{inject} \le 1\%$. The effect of condensation strengthens considerably due to the sloshing (see Section 5).

2.3. Evaporation near the wall-liquid-gas interface

The hot injected GHe or GH2 heats the tank wall causing heat flow along the wall. This flow will induce evaporation of liquid near the wall-liquid-gas interface (Fig 2-7). The heat flow is Given by the following expression:

$$Q_{WL} = 2\pi R_t d_w \left(K_W \frac{dT}{dx} \right)_{/\text{interface}} \approx 2\pi R_t d_w K_W(T_s) \frac{(T_{ws} - T_s)}{\Delta d_{ws}} \tag{18}$$

The evaporation flow $J_{evap,w}$ and the evaporated mass $M_{evap,w}$ near the wall-liquid-gas interface can be estimated from the heat balance equation

$$J_{evap,w} q_L = 2\pi R_t d_w K_w(T_s) \frac{(T_{ws} - T_s)}{\Delta d_{ws}}, \; J_{evap,w} = \frac{2\pi R_t d_w K_{ws}}{q_L} \frac{(T_{ws} - T_s)}{\Delta d_{ws}}, \; M_{evap,w} = \int J_{evap,w} dt \tag{19}$$

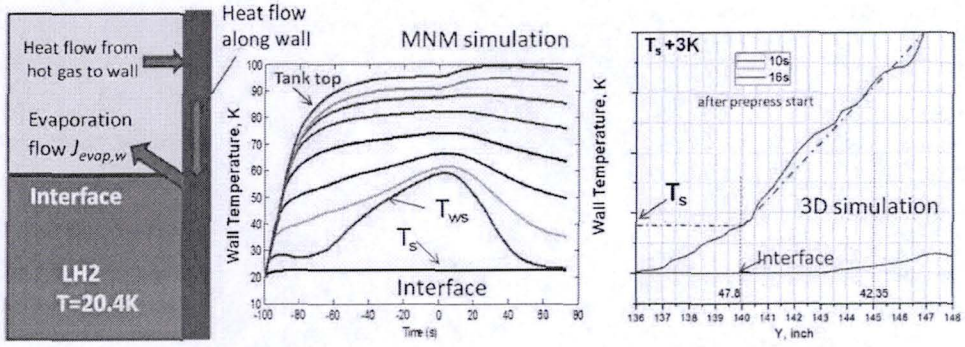

Fig. 2-7 Heat and mass evaporation flows near the wall-liquid-gas interface (left); Wall temperature stratification (results of 3D, in center, and of MNM, right, simulation).

It follows from the MNM and 3 D simulation $\left(K_W \frac{dT}{dx} \right)_{/\text{interface}} \le 4000 \frac{W}{m^2}$ [$(T_{ws} - T_s) < 30K$, $K_{ws} \approx 17 W/m/K$ and $\Delta d_{ws} > 0.15m$]. Therefore, according to Eq. (19)

$$J_{evap,w} < 0.8 g/\text{sec}, \quad M_{evap,w} < 0.04 kg \text{ during the prepress} \tag{20}$$

Note that the total mass of gas in the ullage is greater than 16kg. The condensed vapor mass accumulated during the prepress is ~ 0.4kg (see Sec. 2.1). Thus the effect under consideration is negligibly small during the flight due to $T_{ws} \to T_s$ (Fig. 2-7, right).

2.4. Heating of the tank wall by the hot gas: the main mechanism of the gas cooling

The heat flow from the hot gas in the ullage at T_g to the tank wall at T_w can be written as

$$\dot{q}_{gw} \equiv \frac{dq_{gw}}{dt} = h_{gw}(T_g - T_w),\ h_{gw} = \frac{0.15}{x} K_g(T_g)\left(Ra_x\right)^{1/3} \approx 25\frac{W}{m^2 K},$$
$$Ra_x = \frac{g\beta_{gT} C_g \rho_g(p,T_g)(T_g - T_w)x^3}{\mu_g K_g(T_g)},\ \Psi = \left(1+\left(\frac{0.492}{\mathrm{Pr}}\right)^{9/16}\right)^{-16/9}. \quad (21)$$

Here we use the correlation formulas for the turbulent regime (see Section 4.2.1) as the Rayleigh number $Ra_x > 3\times 10^{10}$ and $Re_x > 10^5$ for x>1m. The heat transfer coefficient h_{gw} and the temperature length $l_{gw} = K_g / h_w$ do not depend on x ($l_{gw} \approx 4.5mm$ *for* $p = 2.4atm, T_g = 300K, T_w = 120K$).

The total heat flux is

$$\frac{dQ_{gw}}{dt} = h_{gw}(T_g - T_w)\delta S_{ul}(t) = d_w C_w(T_w)\rho_w \delta S_{ul}(t)\frac{dT_w}{dt},$$
$$\frac{dT_w}{dt} = \frac{(T_g - T_w)}{\tau_{gw}(T_w)}, \quad \tau_{gw}(T_w) = \frac{C_w(T_w)\rho_w d_w}{h_{gw}}. \quad (22)$$

The temperatures of the ullage and the tank wall depend on the coordinate x along the wall. For the numerical simulations the temperature dependences of the specific heat C_w and thermal conductivity for Al-Li 2195 alloys have been used. The changes in the temperature of ullage gas and in the temperature of the tank wall during the prepress are shown in Fig.2-8. The solid lines are plots of MNM-simulated time-traces of temperatures near the top (upper red curve) and bottom of the tank (blue). The wall temperature $T_w(t)$ increases quickly during the initial stage due to the small value of $C_w(T_L)$=*18J/kgK at T=23K* that increases strongly to 840J/kgK at T=255K.

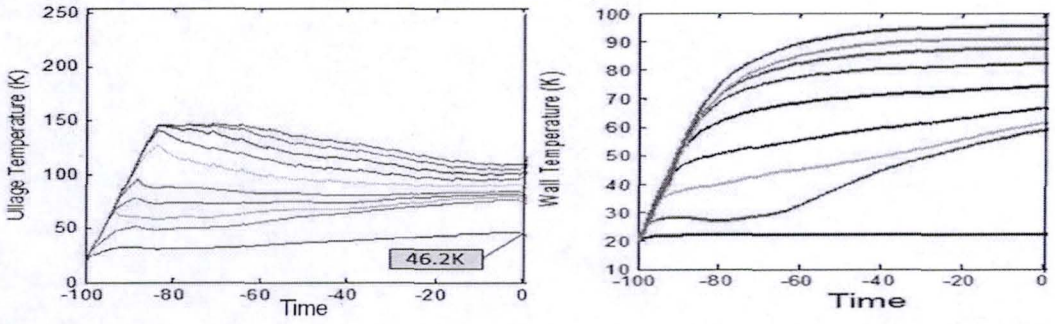

Fig. 2-8 Time traces of the ullage and wall temperature during the prepress.

Heating of the tank wall is the main mechanism of the hot gas cooling in the ullage.

3. Ullage pressure and temperature stratification

3.1. Fitting of the MNM and He pulses parameters to the Space Shuttle data

The values of main parameters at the end of replenish (EOR) stage and at the engine start command (EST) are shown in Table 1 (from [1]). The variation of ullage pressure during the period, t = -103sec to t = 100, is shown in Fig. 3-1 [1]. The pre-pressurization starts at $t^{(0)}_{prepress} = -102.8\,\mathrm{sec}$ with injection of the hot He and finishes at t=-86.5sec. The nominal He flow rate is J_{He}=1.3lb/sec =0.6kg/sec and He temperature is T= 572.4R=318K. The nominal parameters of supply of gaseous He or H2 for STS -115 are presented in Table 1.

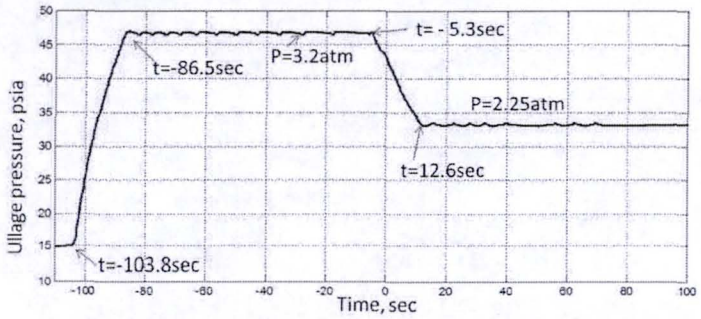

Fig. 3-1. Time traces of the ullage pressure

Table 1: Nominal LH2 tank (STS 115)

EOR		
Ambient Pressure:	1.024atm	14.65 psia †
Ullage Pressure:		0.20 psig
Ullage Pressure:		14.85 psia
Liquid Level:		1044.6 Xt
Ullage Volume:	10.5m³	372 ft³
Ullage Mass:		27 lb_m
Total Tank Volume:	1498m³	52,915 ft³
Bubble Volume:	1.65m³	58.25 ft³
Liquid Volume:	1486m³	52,484 ft³
Vented LH2 Density:		4.41253 lb_m/ft^3
LH2 Propellant Load:		231,588 lb_m

Maximum He flow J_{He}=1.3lb/sec=0.6kg/sec

Maximum H2 flow J_{H2}=3x0.35lb/sec=0.476kg/sec

ESC Through T-0		
LH2 Losses Prior to ESC:		113 lb_m
Ullage Pressure:		32.35 psig
Ullage Pressure:	3.24atm	47 psia
GHe (Anti-Ice) Mass Added:		1 lb_m
GHe (Prepress) Mass Added:		38 lb_m
Ullage Volume @ ESC	27.15m³	959 ft³
Ullage Mass @ ESC		68 lb_m
ET Liquid Volume @ ESC		52,320 ft³
ET Liquid Mass @ ESC		231,475 lb_m
Press'd LH2 Density		4.42427 lb_m/ft^3
Predicted LH2 Usage to T-0:		1,792 lb_m
LH2 Transferred to SSMEs:		58 lb_m
Loaded LH2 at T-0:		229,625 lb_m
Predicted Ullage Volume - % of Liquid Volume		1.83
Required Ullage Volume - % of Liquid Volume		1.54

The ullage pressure drops at $t \geq t^{(0)}_{prepress}$ due to cooling of the hot injected He (see Sec. 2.3) and expansion of the ullage volume under the pressure increase. Pulses of He injection are applied when the ullage pressure drops below the threshold value of p_{th} =20.54 psig=35.2psia. The form of the He mass flow pulses is shown in Fig. 3-2. In more detail, the pulses have amplitude j_{He} *=0.3lb/sec=0.136kg/sec* and their form is given by:

$$j(t) = j_{He}\begin{cases} 1-\exp\left(-(t-t_i)/\tau_{front}\right), & t < t_i + \tau_p \\ \exp\left(-(t-t_i-\tau_p)/\tau_{tail}\right), & t > t_i + \tau_p \end{cases} \qquad (23)$$

where at $t=t_i$ the ullage pressure drops to the threshold value of p_{th} and i-pulse is generated.

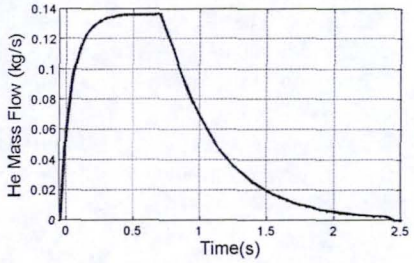

Fig. 3-2: The form of the He mass flow pulses.

Ullage temperature stratification and gas velocity distribution during the first stage of the prepress found in 3D simulation are shown in Figs. 3-3 and 3-4. Temperature distributions during the prepress and first stage of the flight are shown in Fig. 3-5. One can see that temperature smoothly decreases from the high temperature near the tank top (T≈300K) to the low temperature at the interface (T≈23K) during the prepress, and the temperature distributions becomes more pronounced during the flight (Fig.3-5).

We chose a single fitting parameter of MNM, numerical coefficients β_u in the velocity correlation for the turbulent natural convection (see Eg. (25)), in such a way as to fit the temperature distribution found in the 3D simulation (Figs. 3-3 - 3-5). The sawtooth modulations of the ullage pressure induced by the He pulses were fitted to the telemetric data. For the fitting we chose parameters of He impulses in Eg. (23) (The pulse duration τ_{pulse} and its front and tail durations τ_{front} and τ_{tail}).

$$h_F^{tur} = 0.15\beta_h K_{L/G}\frac{\left(Ra_x\Psi\right)^{1/3}}{x} \propto \beta_h x^0, Ra_x = \frac{g\cos\varphi_t\beta_T C_{L,G}\rho_{L,g}(T_{LW}-T_L)x^3}{\mu_{L,G}K_{L,g}},$$

$$u_{N,x} = \beta_u \overline{u}_N(x), \overline{u}_N(x_i) = 0.178\frac{\nu}{x_i}\left(\frac{Ra_x \Pr}{1+0.494\Pr^{2/3}}\right)^{1/2} \propto \beta_u x^{1/2} or\ \overline{u}_N(x_i) = \left(\frac{g\beta_T q_{env}x}{C_{L,G}\rho_{L,g}}\right)^{1/3} \quad (24)$$

$$j_N = 2\pi R_{\text{tank}}\delta_x u_{N,x}\rho_{L/G} \propto \beta_u x^{6/5},$$

$$\delta_x = 0.565x\left[\left(1+0.494\Pr^{2/3}\right)/Ra_x\Pr^{23/15}\right] \propto x^{7/10}$$

Amplitude of He mass flow was 1.3lb/sec =0.6kg/sec. The fitting gave the following values for the parameters:

- β_u= 0.2
- τ_{front} = 0.12sec, τ_{tail} = 0.4sec, and τ_{pulse} = 0.4sec

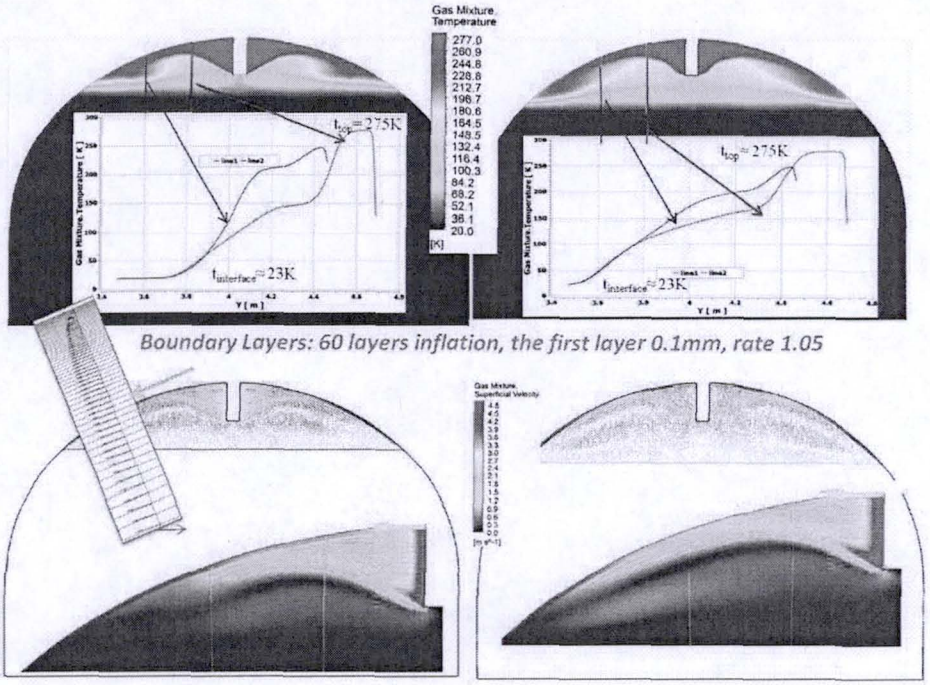

Fig. 3-3: Distribution of the ullage temperature (upper) and velocity (below) during the first stage of the prepress: 3D simulation at t=10sec (left)-and 16sec (right) after the prepress start.

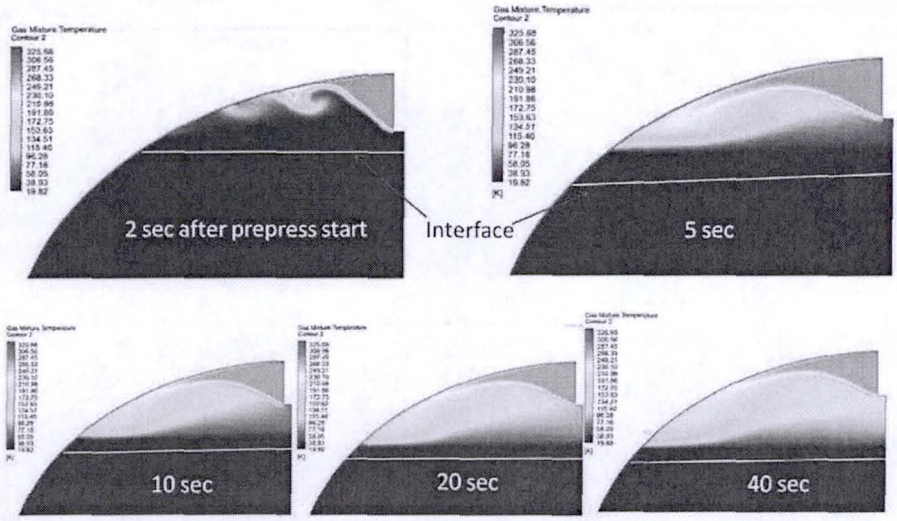

Fig. 3-4: Temperature stratification during the prepress: Results of the 3D simulation for different times after the beginning of prepress.

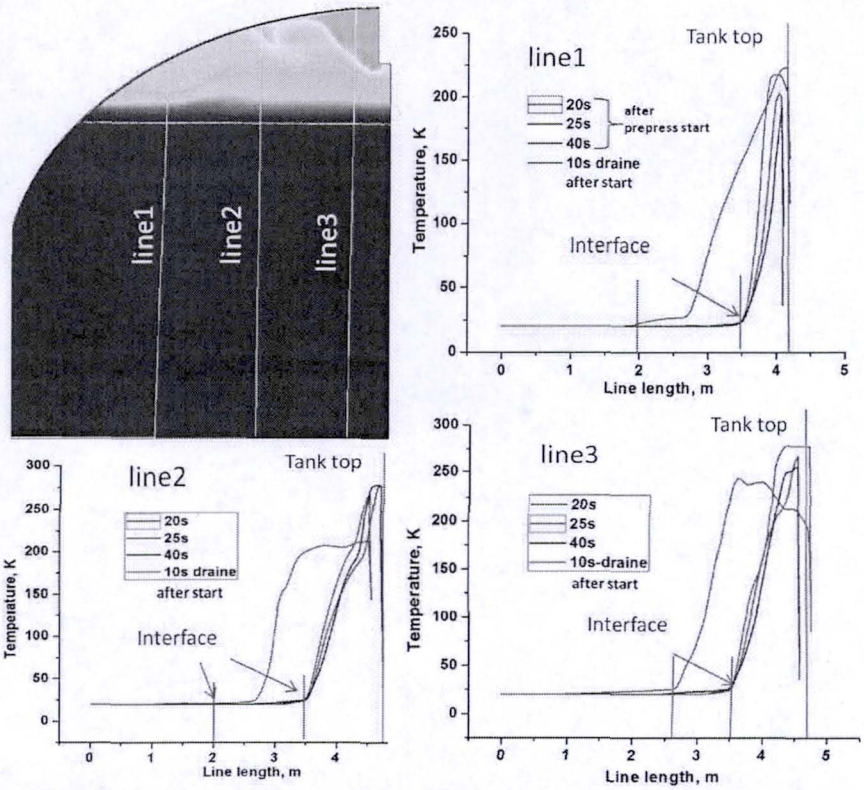

Fig. 3-5: Temperature stratification during the prepress and the first stage of the Shuttle flight: Results of 3D simulation for different times after prepress start.

Stratification of the ullage and wall temperature found in a MNM simulation is shown in Fig. 3-6. Results of fitting time-traces of the ullage pressure and temperature near the tank top, where the thermo-sensor is located, are shown in Fig. 3-7. We see that the results of the MNM simulations fit well the STS-115 data. We emphasize that the only fitting parameter of the MNM was the numerical coefficient β_u in the correlation relation for the natural convection velocity (Eq. (24)). This coefficient depends on the fluid's properties and is essentially independent on the tank design. Therefore we used MNM with this fitting parameter for analysis of the rescaled LH2 SLS tank.

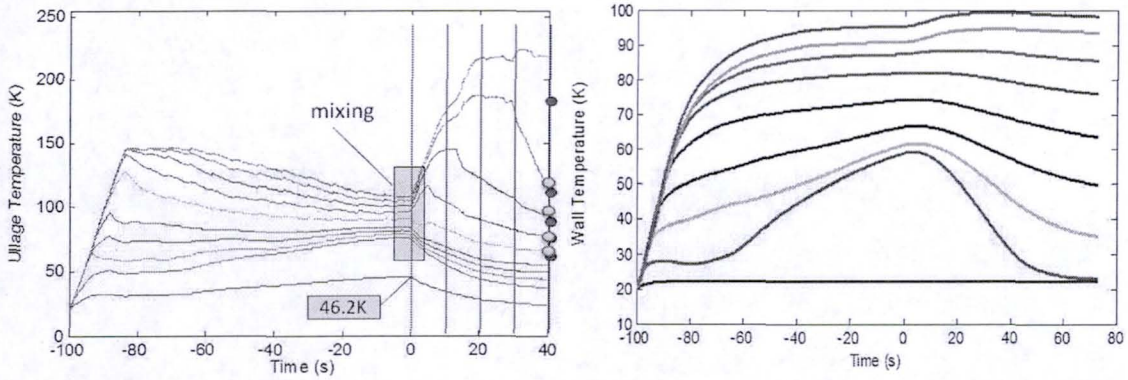

Fig. 3-6. Stratification of the ullage (left) and wall temperature (right) during the pre-press and the initial stage of the flight. Results of the MNM simulation.

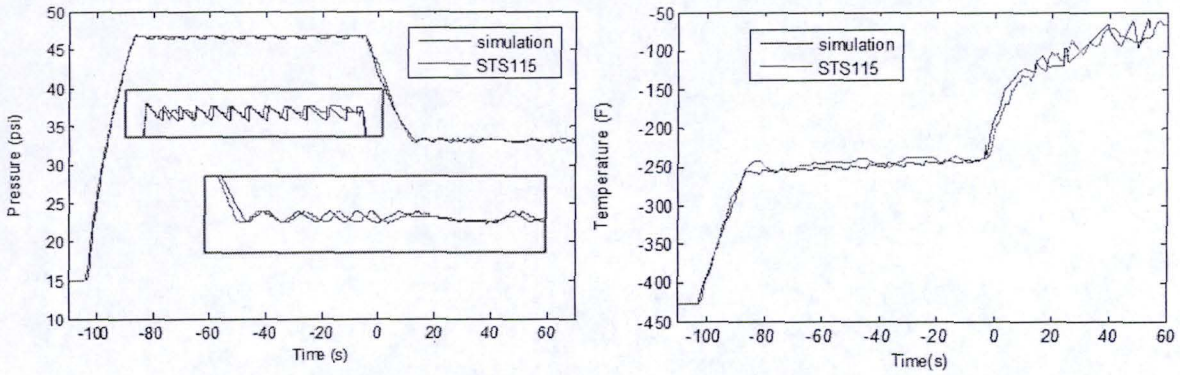

Fig. 3-7: Time-traces of ullage pressure (left) and ullage temperature (right) near the tank top during the pre-press and the initial stage of the flight. Results of MNM simulation.

3.2. Scaling considerations for the LH2 tank for SLS with 5 engines

The MNM with fitting parameter β_u= 0.2 are further used in modeling the prepress and fight regimes for the proposed design of the SLS LH2 tanks to assess the associated risks. Results of these simulations for 5/3 scaling SLS tank are shown in Figs. 3-8 and 3-9. Fig. 10 illustrates the ullage temperature distribution in 5/3 scalable SLS Lh2 tank found from 3D simulation for prepress stage. We increased the mass flows of injected He and GH2, and also ullage volume and tank volume, due to its extension, in 5/3 times.

It can see from comparison of Figs. 3-4 and 3-6 with Figs. 3-8 and 3-10 that the temperature stratification is more pronounced in the 5/3-rescaled SLS LH2 tank due to a lesser mixing of the initial cold and injected hot gases. Results presented in Figs.3-7 and 3-9 indicate that the time traces of the ullage pressure in Space Shuttle tank and in 5/3-rescaled LH2 tank are close. However the numbers of the sawtooth variations of the ullage pressure initiated by injection of He impulses during the prepress are different because of difference in the GHe masses and surfaces of the tank wall corresponding to the ullage volumes in Space Shuttle and SLS tanks.

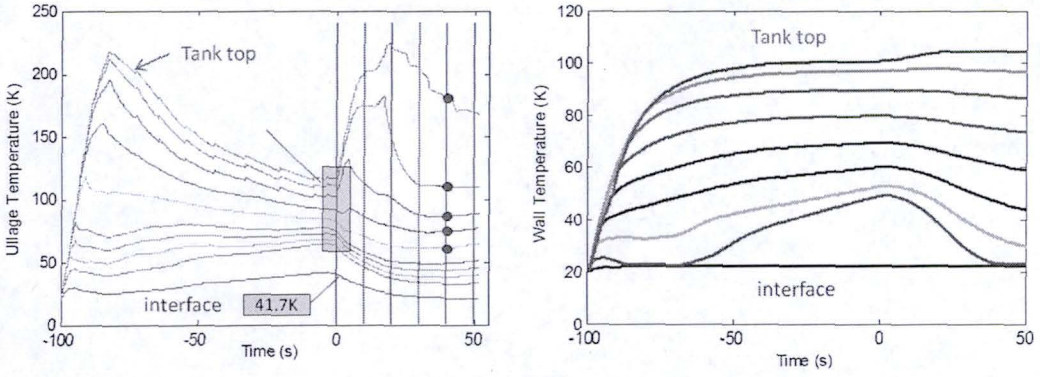

Fig. 3-8. Stratification of the ullage (left) and wall temperature (right) during the pre-press and the initial stage of the flight for 5/3 scalable SLS Lh2 tank. Results of MNM simulation.

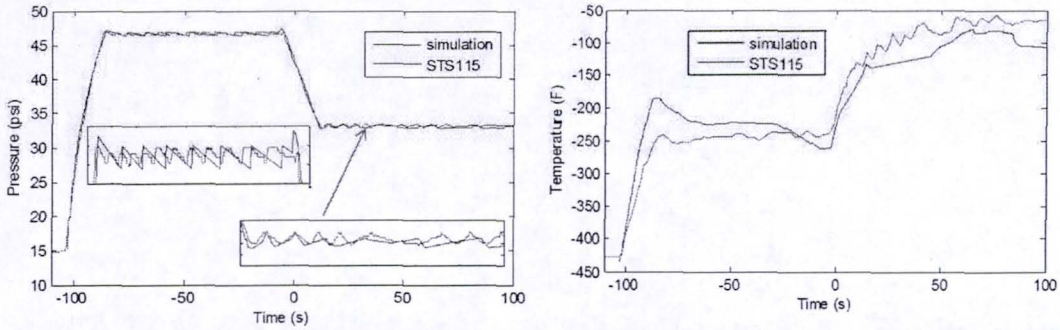

Fig. 3-9: Time-traces of ullage pressure (left) and ullage temperature (right) near the tank top during the pre-press and the initial stage of the flight for 5/3 scalable SLS LH2 tank. Results of the MNM simulation.

We see that the observed time trace of the ullage pressure for SLS 5/3-rescaled LH2 tank falls within the permitted bounds (see Fig. 3-11)

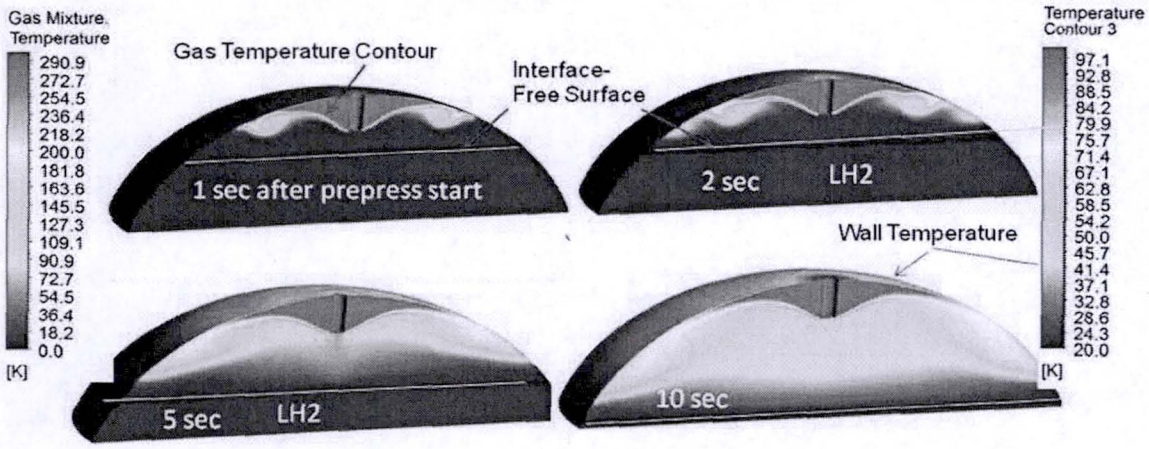

Fig.3-10: Temperature stratification in 5/3 scalable SLS Lh2 tank: Results of 3D simulation for different times after the beginning of the prepress.

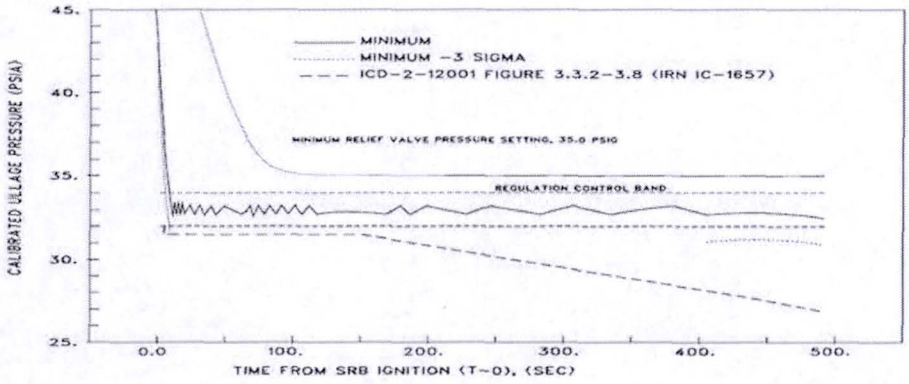

Fig. 3-11. Requirements to the ullage pressure [1]

4. Temperature stratification in the liquid

The temperature stratification patters in the tank is shaped by two main physical processes: (i) condensation-evaporation on the gas-liquid interface and (ii) natural convection along the tank wall (Figure 4-1).

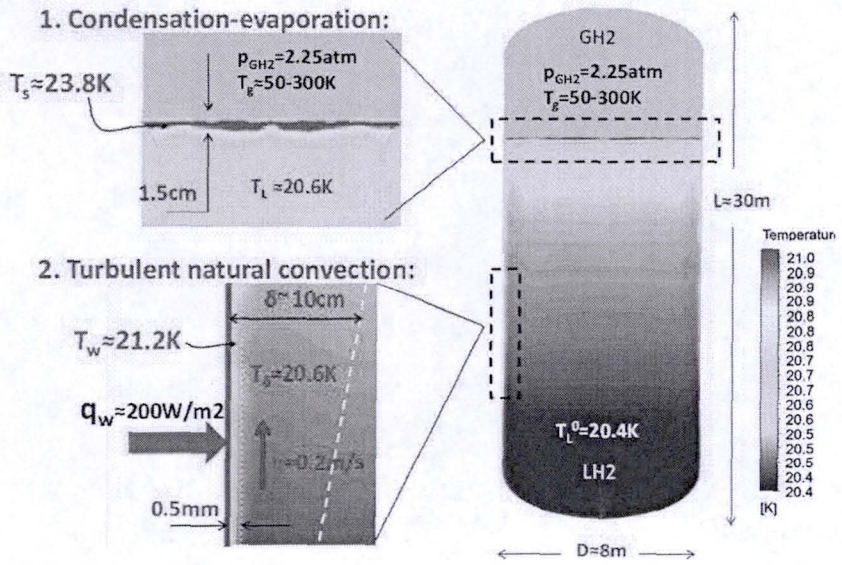

Fig.4-1. Physical processes contributing to the temperature stratification in cryogenic tank

4.1 Heating of liquid in the boundary layer near the gas-liquid interface

The liquid layer near the liquid-gas interface is heated due to condensation. The surface liquid temperature is determined by the partial pressure of H2 vapor p_{GH2} near the interface (Eq. (9)). It can be seen from Fig. 2-6 that the partial GHe pressure near the interface p_{GH2}<32psi=2.25atm. Therefore, the surface liquid temperature, according to Eq. (9), is $T_s \le$ 23.8K (T_s-$T_L \le$ 3.4K). The width of this overheated liquid layer is determined by the thermodiffusion length (Fig. 4-1) of the liquid (Eq. (11)) which increases with time and approaches a value of $L_{DL} = 1.5cm$ toward the end of the flight. This conclusion explains results of 3D simulation presented in Fig. 4-2 that shows temperature stratification in the liquid near the interface in the end of the flight (t_{flight}=500sec).

The upper bound for the mass of the overheated liquid in this layer can be estimated as $M_{warm} \approx 0.5S(t_{flight})\rho_L L_{DL}(t_{flight}) = 30kg$ while the total LH2 mass in the filled tank is 105,000kg.

The heat flow into the liquid associated with the condensation is given by

$$\dot{Q}_L - \frac{dQ_L}{dt} = K_L \frac{(T_s - T_L)}{L_{DL}(t)} S_L(t) = (T_s - T_L) S_L(t) \sqrt{\frac{K_L C_L \rho_L}{\pi t}} \qquad (25)$$

The total heat associated with the condensation of GH2 is

$$Q_L(t) \approx (T_s - T_L)\bar{S}_L \sqrt{K_L C_L \rho_L (4t/\pi)}, \quad Q_L(t_{\text{flight}}) \approx 5 \times 10^5 J \qquad (26)$$

while the total heat of GH2 injected during the flight (t_{flight} =500sec) is

$$Q_{ullage} = C_{vOx} M_{GOX} T_{ullage} = C_{vOx} \frac{p_{ullage} V_{\tan k}}{R_{Gox}} = \frac{p_{ullage} V_{\tan k}}{\gamma - 1} = 2.5 \cdot 10^8 J \quad (27)$$

$$Q_{inject} = C_{pOx} T_{inj} J_{inj} t_{flight} = 3.4 \cdot 10^8 J, J_{inj} = 1.3 kg / \sec, \; T_{inj} = 800R = 444K$$

Thus, the additional heat of this overheated layer has a relative small value: $Q_L(t_{flight}) / Q_{inject} = 0.1\%$.

4.2 Heating of liquid in the boundary layer near the wall

4.2.1. Natural convection correlations

There is a constant heat flow across the tank wall q_w~200W/m^2 . The natural convection flow generated by this heat is highly turbulent in a large tank such as LH2 tank. With characteristic Reynold number Re~10^6 . As a consequence a theory dealing with the natural convection in the tank is a theory of turbulent flows. Due to the notorious closure problem (Figure 4-2) little progress can be done by a rigorous mathematical analysis of the equations of motion and additional physical assumptions have to be made which cannot by derived from the equations of motion and the boundary conditions. These assumptions have to be validated by comparison of the theoretical predictions with the experiment. We note that the results of this subsection are applicable to natural convection in both the liquid and the ullage space, provided the Boussinesq approximation (Figure 4-2) hold.

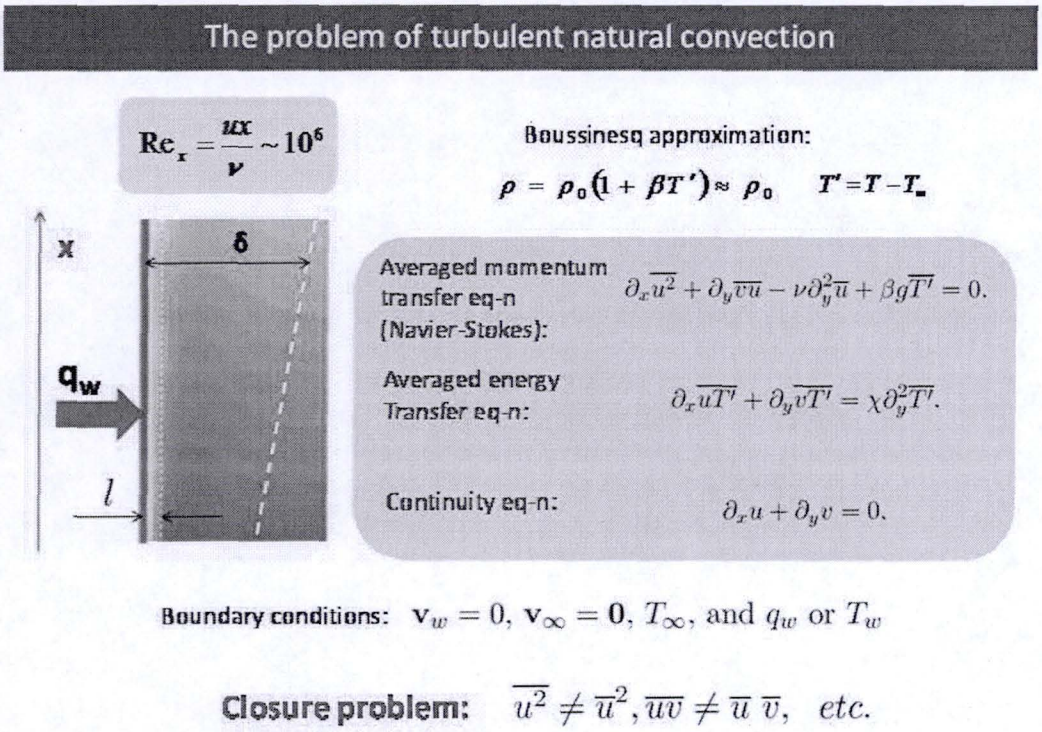

Fig.4-2. The closure problem for the turbulent flow

In contrast to the forced convection there seems to be no consensus in the literature about what are the correct assumptions for the natural convection theory [11-16]. In what follows we outline the physical picture which is correct in our opinion, derive certain correlation relations based on this picture and validate the predictions by comparison to experimental evidence and high fidelity simulations which we believe to be correct.

To set up the stage for the discussion, let's consider Figure 4-3, which depicts a turbulent flow near the wall due to the natural convection. One should distinguish two characteristic length-scales of this flow: the viscous or conduction length-scale l, and the turbulent length scale δ. The former lengh-scale corresponds to the inner sublayer of the flow, where the heat and momentum are transferred by thermodiffusion and viscous fiction, respectively (for LH2 the Prandtle number is ~1, therefore both the thermal diffusion and the viscous friction are characterized by the same length-scale).

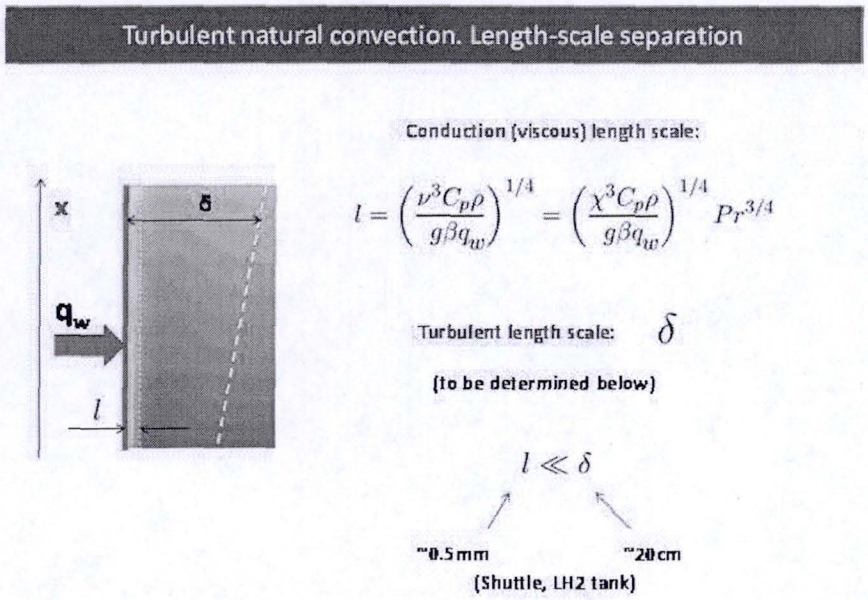

Fig.4-3. Length-scales separation in the turbulent natural convection

The latter length-scale, δ, corresponds to the outer region of the turbulent boundary layer, where the transport of both heat and momentum is carried out by the turbulent pulsations. For well-developed turbulent flow as in the LH2 tank, there is a huge separation between the two length-scales with ratio $l/\delta \sim 10^{-3}$.

The turbulent heat and momentum transport is highly efficient. Therefore, we expect that the all the heat absorbed by the viscous sublayer from the wall is transferred into the outer turbulent sublayer (Figure 4-4). This is a very powerful assumption and it leads to very different results from those obtained by assuming that rather the total momentum flux from the wall is transferred into the outer sublayer, as happens in forced convection and as was assumed in an influential paper by Eckert and Jackson [12].

Assuming the heat flux q_w into the outer region, where the microscopic (as distinguished from the turbulent) viscosity and thermo conductivity are negligible, we are left with the following physical variables which can determine the characteristic velocity and temperature scales in the outer region: heat flux, q_w, gravity acceleration g, volumetric expansion coefficient, specific heat C_L , density ρ and streamwise coordinate along the wall x. Out of these variables one can build just a single velocity scale u and a single temperature scale $T' = T - T_\infty$ (T_∞ is the temperature in the bulk of the liquid far away from the wall) [13]:

$$u = A\left(\frac{q_w g\beta x}{C_L \rho}\right)^{1/3}$$
$$T' = B\left(\frac{q_w}{C_L \rho}\right)^{2/3} (g\beta x)^{-1/3} \qquad (28)$$

where A and B are empirical constants, which have to be determined from an experiment. Remarkably, the temperature is seen to decrease streamwise! This counterintuitive prediction can be understood if one realizes that the heat absorbed from the wall is diffused by the

turbulent pulsations in ever increasing width of the turbulent outer layer δ down the stream, leading to a smaller temperature increase per same heat absorbed.

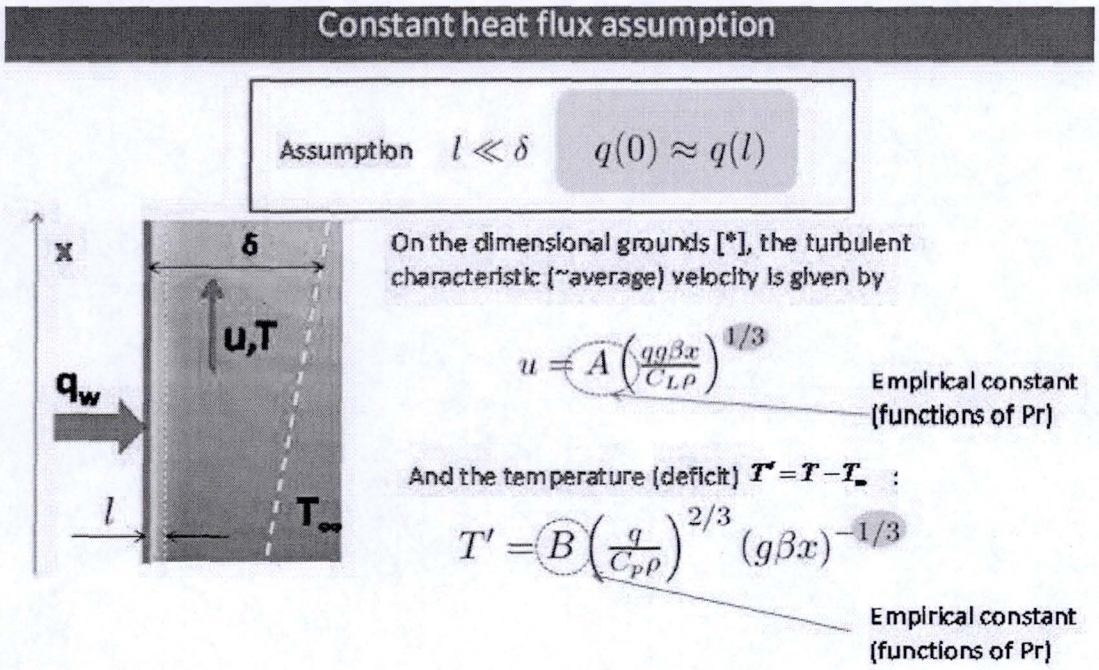

Fig.4-4. Assumption of constant heat flux into the outer turbulent region.

To calculate the actual x-dependence of δ we consider the heat balance for a certain control volume in the boundary layer (Figure 4-5):

$$q_w x \approx C_L \rho u T' \delta \tag{29}$$

Eqs.(29-30) imply that the width of the outer region grows linearly with the streamwise coordinate x, δ~x. This fast growth explains the decrease of the characteristic temperature in the turbulent region with the height of the tank x.

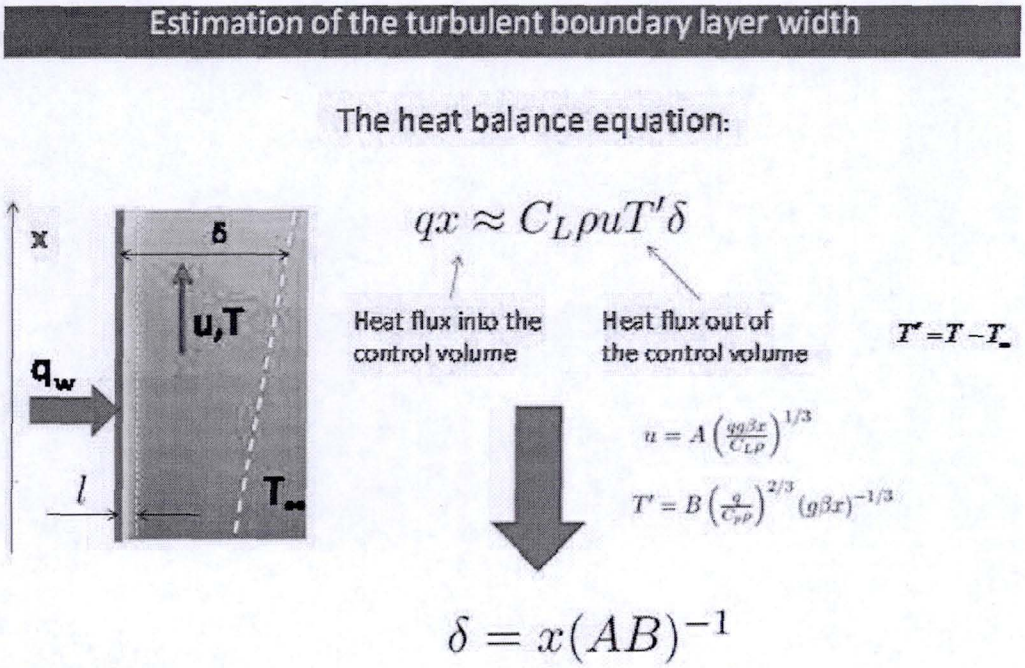

Fig.4-5. Estimation of the turbulent boundary layer width.

A very important consequence of the predicted streamwise temperature decrease is that the main temperature change occurs in the inner conductance region of width l_w. In fact, near the wall the temperature changes linearly with the distance from the wall y:

$$\frac{q_w}{C_L \rho} \approx \kappa \frac{\partial T}{\partial y} \tag{30}$$

So the change of the temperature over the width l_w of the conductance region

$$\Delta T \approx \frac{q_w l_w}{C_L \rho \kappa} \tag{31}$$

is independent of x, i.e., for sufficiently large x it becomes much larger than the characteristic turbulent outer region temperature scale $T' \sim x^{-1/3}$. It follows that for large x the temperature of the wall is $T_w \approx \Delta T + T_\infty$, which sets the characteristic scale of the temperature in the conductance region. This is a very important conclusion which means essentially the temperature increase of the boundary layer due to the heat flux is independent of the height of the tank for sufficiently large tanks (Figure 4-6).

The foregoing argument can be considered as a theoretical justification of the constant heat transfer coefficient for the natural convection h, which is a very well established empirical correlation relation, known in the literature [17]:

$$
\begin{aligned}
q_w &= h\left(T_w - T_\infty\right) \\
h &= 0.15\kappa\left[Gr_l \,\mathrm{Pr}\left(1+\Psi\left(\mathrm{Pr}\right)\right)\right]^{1/3} \\
Gr_l &= \frac{g\beta\left(T_w - T_\infty\right)}{\nu^2} \\
\mathrm{Pr} &= \nu/\kappa \\
\Psi(\mathrm{Pr}) &= \left[1+\left(0.492/\mathrm{Pr}\right)^{9/16}\right]^{-16/9}
\end{aligned}
\tag{32}
$$

An important contribution of our theoretical analysis is assertion that not only is the wall temperature constant for the constant heat flux turbulent natural convection, but that the heating essentially occurs in the conductance sublayer only, i.e., that $\Delta T = T_w - T_\infty$. This latter property allows one to calculate not only the characteristic temperature in the inner sublayer but its width, too, which is important for the stratification analysis.

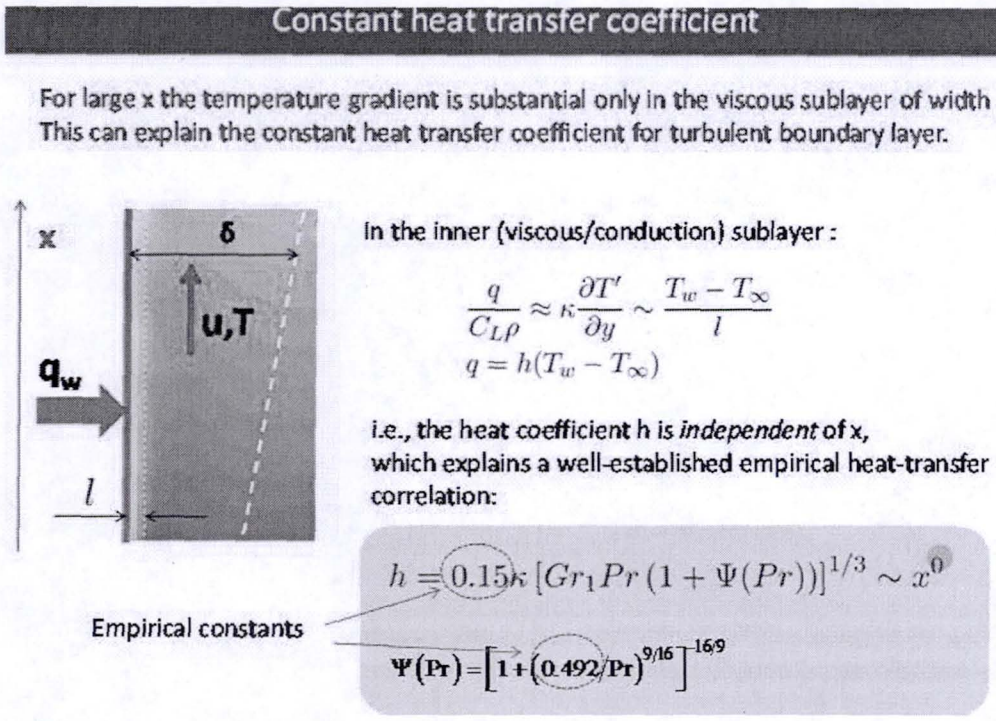

Fig.4-6. Constant heat transfer coefficient.

The precise value of the temperature drop near the wall $\Delta T = T_w - T_\infty$, including the numerical factor, can be calculated using the empirical expression for the heat transfer coefficient (33).

To summarize the main predictions of the foregoing theoretical arguments:

- The absorbed heat is accumulated in the turbulent outer sublayer
- The width of the turbulent sublayer increases streamwise
- As a consequence the average temperature in the turbulent sublayer decreases streamwise

- The temperature gradient is substantial in the conductance (viscous, inner) boundary sublayer
- The temperature is streamwise constant in the conductance boundary sublayer

The important implication of these predictions, if proved (experimentally/numerically) correct, for the temperature stratification in the tank is the following: The temperature of the warm layer accumulated beneath the gas/liquid interface is independent of the tank height. In other words, the temperature stratification pattern is essentially invariant with respect to the tank rescaling. By "essential" we mean heating which is likely to be of any consequence from the Net Positive Suction Pressure Condition (NPSP) perspective.

Now we precede to validation of the correlation relations by comparing our predictions to experiments and high fidelity simulations. In 1988 a series of experiments on the natural convection in the air (Figure 4-7) has been published in Refs. [14-15], which is considered one of the most reliable data on the natural convection to date.

Validation of correlations. Comparison to experimental data.

Natural convection of air along a vertical flat plate

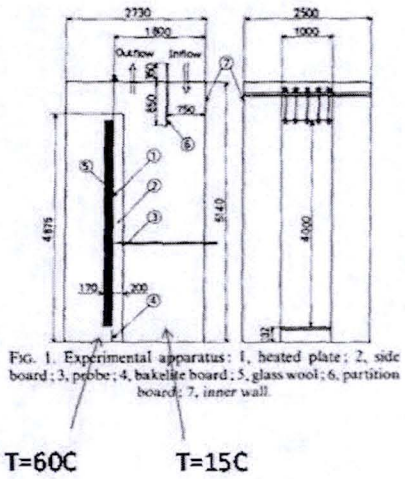

FIG. 1. Experimental apparatus: 1, heated plate; 2, side board; 3, probe; 4, bakelite board; 5, glass wool; 6, partition board; 7, inner wall.

•T. Tsuji and Y. Nagano, "Characteristics of a Turbulent Natural Convection Boundary Layer along a Vertical Flat Plate", Int.J Heat Mass Transfer, 31, pp. 1723-1734 (1988).
•T. Tsuji and Y. Nagano, "Turbulence Measurements in a Natural Convection Boundary Layer along a Vertical Flat Plate", Int.J Heat Mass Transfer, 31, pp. 2101-2111 (1988).

Fig.4-7. Turbulent natural convection in the air. Experimental setup.

A large vertical copper plate was heated to T=60°C, while the surrounding air was held at T=15°C. The air was entrained from beneath by the turbulent convection and raised along the wall where the hot wire detectors were placed, measuring the temperature and velocity distribution. We have simulated the experiment and plotted the results against the experimental data (Figure 4-8).

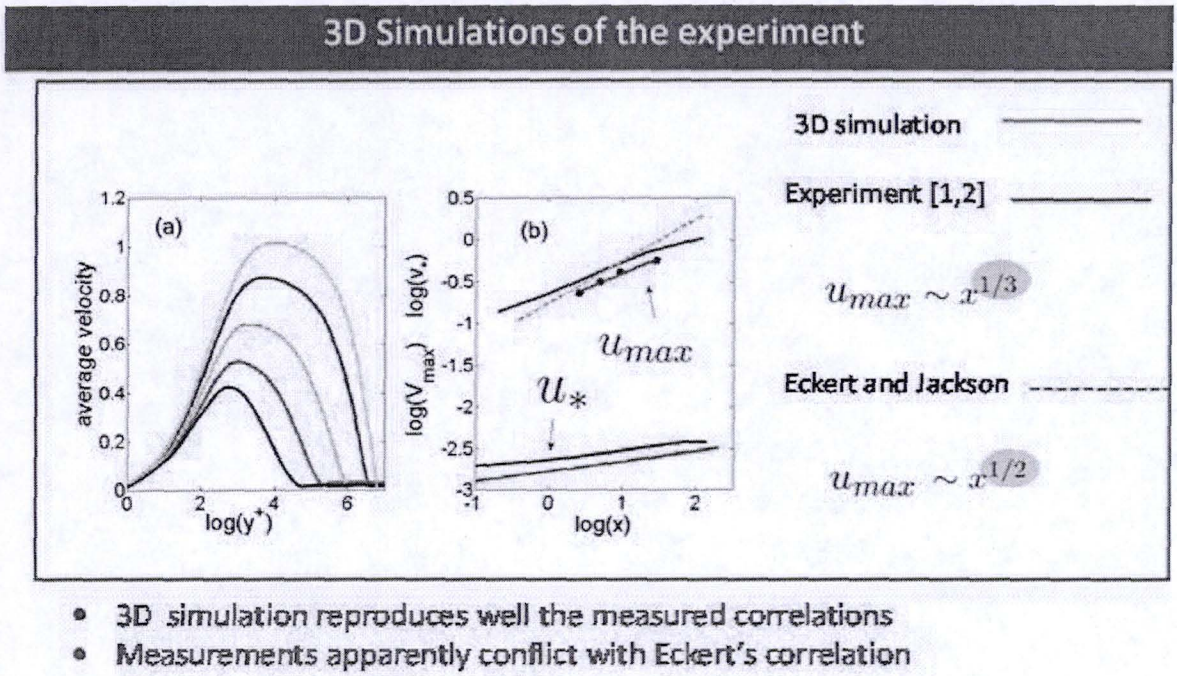

[1] T. Tsuji and Y. Nagano, "Characteristics of a Turbulent Natural Convection Boundary Layer along a Vertical Flat Plate", Int.J Heat Mass Transfer, Vol. 31, No 8, pp. 1723-1734 (1988).
[2] T. Tsuji and Y. Nagano, "Turbulence Measurements in a Natural Convection Boundary Layer along a Vertical Flat Plate", Int.J Heat Mass Transfer, Vol. 31, No 10, pp. 2101-2111 (1988).
[3] E. R. G. Eckert and T. W. Jackson, Analysis of Free-Convection Boundary Layer on Flat Plate, National Advisory Committee for Aeronautics technical memorandum No. 2207, Washington, September 1950

Fig.4-8. Turbulent natural convection in the air(High fidelity simulation).

In addition, comparison to the predictions of Ref. [12] has been performed. The comparison is particularly important in view of the fact that correlations proposed in Ref.[12] have been widely used in NASA related research for computation of stratification in tanks [18-22]. The results (Fig. 4-8) demonstrate a good correspondence of experimental data to our numerical simulations, supporting the predicted $x^{-1/3}$ scaling of the characteristic velocity, Eq.(29). The scaling predictions of Ref. [12] are clearly at odds with these results.

The next piece of validation comes from simulation of the natural convection of GO2 in a large cryogenic tank (Figure 4-9). The walls of the tank were kept at T=90K, while the bulk temperature of the gas was T=100K. There results of the simulation are plotted on Figure 4-10. We see that the predicted $x^{-1/3}$ scaling of the characteristic velocity, Eq.(29) is confirmed by the results of the simulation.

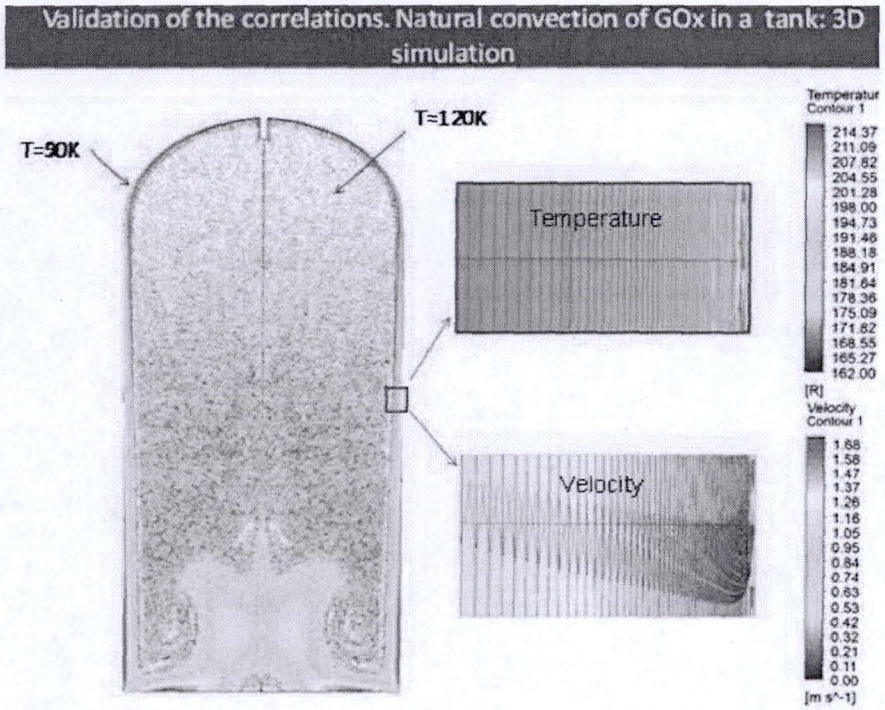

Fig.4-9. Natural convection of GO2 in a cryogenic tank. High fidelity simulation.

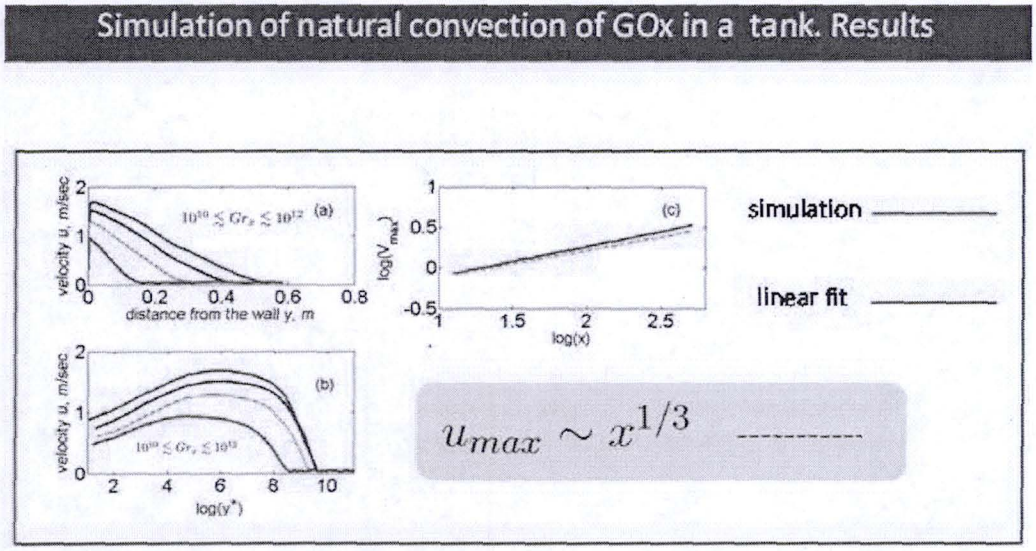

3D simulations support the predicted scaling of the characteristic velocity

Fig.4-10. Natural convection of GO2 in a cryogenic tank. High fidelity simulation results.

4.2.1. Natural convection in the LH2 tank

As the further step toward the problem of the temperature stratification in the LH2 tank we performed the simulation of the temperature and velocity profiles of the turbulent boundary layer flow for the natural convection in LH2 tank (Figure 4-11). The initial (and the bulk) temperature of LH2 was taken T_∞=20.4K. The temperature of the gas-liquid surface (1.4 m from the top of the tank) was kept at Ts=23.8K, which corresponds to the partial GO2 pressure in the ullage p_{GO2}=2.25atm. The heat flux through the wall was q_w=200W/m^2. The simulation was performed for liquid dynamics over 500 sec. At t=50sec after the beginning of the heating, the turbulent natural convection flow is expected to have developed. The estimate for the characteristic time τ of the turbulent flow development is $\tau \sim \delta / u_* \sim 10\text{sec}$, where δ~10cm is the boundary layer width and u_*~1cm/sec is the scale of turbulent velocity pulsations as measured in the simulations.

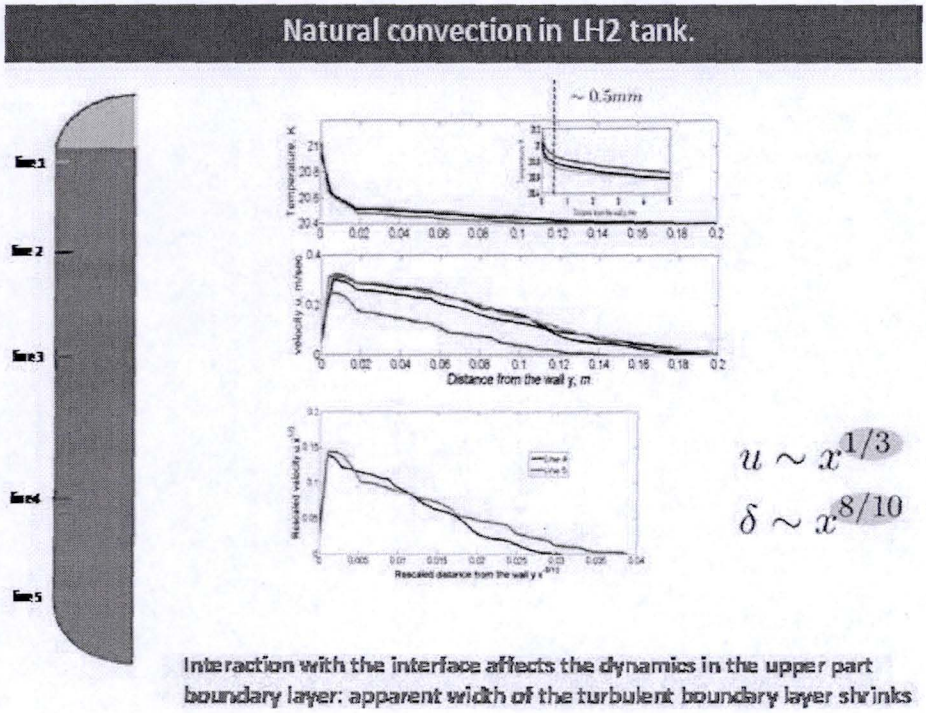

Fig.4-11. Natural convection in LH2 tank. Velocity and temperature profiles.

The profile for the temperature in the vicinity of the wall is seen to comply with predictions of the theory : $T_w - T_\infty \approx 0.8K$, as calculated using the known heat flux and correlations (A33), the width $l_w \approx 0.5mm$ as calculated using relation $\Delta T \approx T_w - T_\infty$, Eqs. (31) and (33). Velocity profiles corresponding to lines 4 and 5 on Figure 4-11 are seen to collapse on a single graph after the best-fit rescaling of velocities by $x^{1/3}$ and length by $x^{8/10}$. The latter scaling deviates a bit from the predicted linear dependence of the turbulent outer region width δ, which we attribute the finite Reynolds number effect. However the velocity profiles at lines 1,2 and 3 are seen to deviate substantially from the prediction of the theory, namely, the apparent turbulent outer region width δ is found to saturate at certain value. This deviation could in principle lead to heating the outer layer above the temperature predicted by the correlations (29) and therefore should be examined carefully. The simulation results presented in Figure 4-12, give the clue to the solution. The structure of the turbulent flow in the upper part of the tank is much more complex

than in the asymptotic theory of natural convection, which neglects effect of the boundary – the gas-liquid interface. Due to this effect, at sufficiently large time t, the descending flow starts to develop, which interact with the ascending flow due to the natural convection. We expect that this interaction leads to development of the turbulent shear layer which projects deeply in the bulk of the liquid far beyond the point, where the velocity of the raising flow vanishes. As a consequence, we expect that the actual width of the turbulent flow is much wider than an apparent width in Figure 4-11 as assessed from the raising flow velocity profile

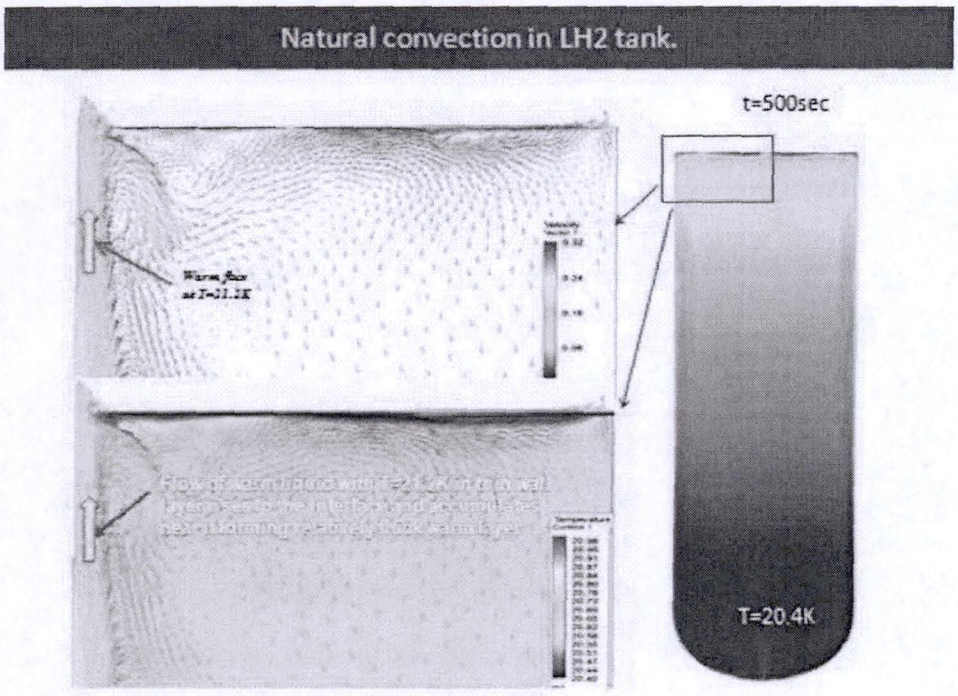

Fig.4-12. Natural convection in LH2 tank. Effects of the liquid-gas interface.

To test our conjecture we numerically computed the distribution of the turbulent kinetic energy near the wall for lines 2 and 3 at t=500sec (Figure 4-13). The results of the simulations show that in fact the turbulence is spread far beyond the zero-velocity point, leading to an efficient heat transport away from the wall. Even if the scaling for this dynamics deviates from the prediction of the asymptotic theory of natural convection, the main physical rational which lies in the basis of (i) the constant heat transfer coefficient law (33) and (ii) prediction that the heating of the liquid is essentially confined to the conductance sublayer of width lw, is still valid. That is, the turbulence efficiently diffuses the absorbed heat in the large volume of liquid, so that the main drop of the temperature takes place in the conductance inner region.

The results of simulation support the foregoing arguments (Figure 4-14): the temperature at the wall, taken at t=500sec is found to stay almost constant along the wall and correspond very accurately to the predicted value $T_w - T_\infty \approx 0.8K$, the characteristic width of the heated sublayer $l_w \approx 0.5$mm corresponds well to the theoretical estimate, too.

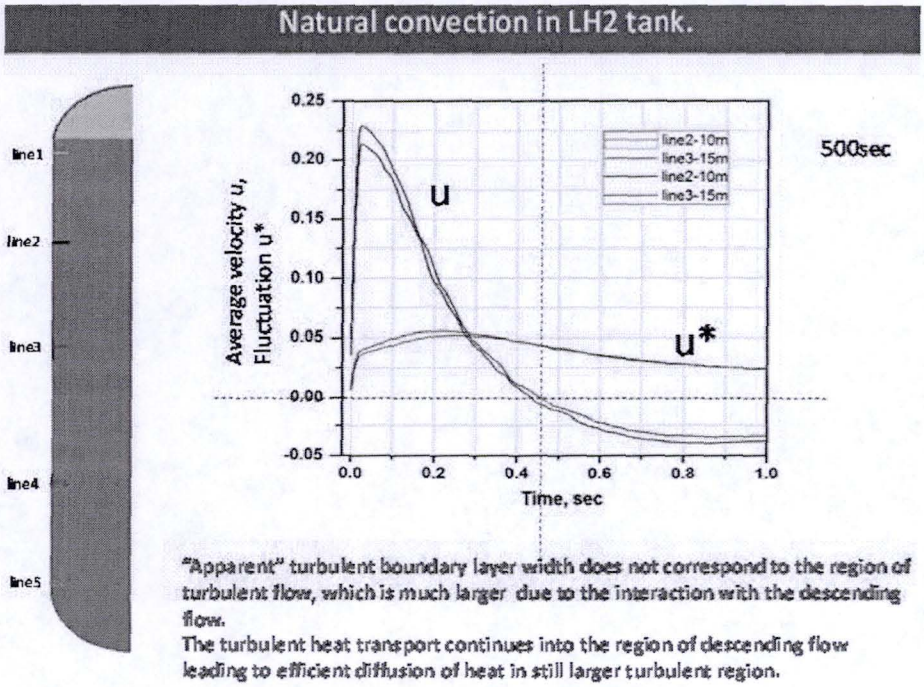

Fig.4-13. Turbulent pulsations vs. average velocity; t=500sec.

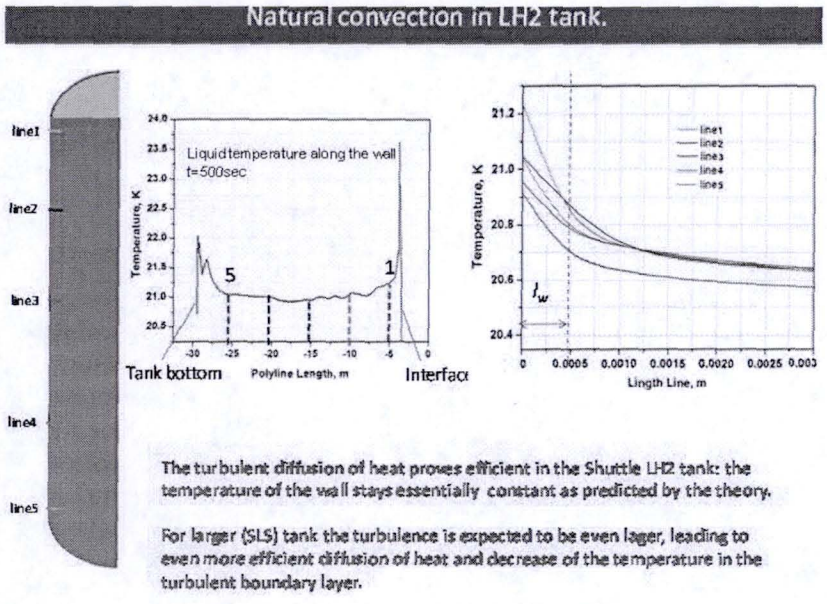

Fig.4-14. Inner sublayer temperature distribution; t=500sec.

4.3 Temperature stratification in the LH2 tank

The foregoing results have important implications for the temperature stratification in the tank. In fact, the ullage pressure is $p_{ull} \approx 33psi = 2.25atm$ during the flight which corresponds to the boiling temperature $T_{boil} \approx 24K$. On the other hand, the predicted near-wall temperature $T = 21.2K$ corresponds to the pressure of saturated vapor $p_{s,vap} = 1.1atm$. The temperature of the

turbulent outer layer is much lower and corresponds essentially to still lower pressure $p_{s,vap}$=1atm. Therefore, the heating of the liquid due to the natural convection does not create a hazard: the Net Positive Suction Pressure condition is satisfied during the flight due to large ullage pressure $p_{ull} \approx 33psi = 2.25atm$. In fact the Net Positive Suction Pressure (NPSP) condition for the LH2 tank reads:

$$p_{ull} + p_{head} - \Delta p_{fric} - p_{s,vap}(T_L(t,x)) > 5psi \tag{33}$$

The hydrostatic pressure p_{head} is negligible for LH2. The frictional pressure drop Δp_{fric} is determined by drop the thinnest segment of the feedline of the RS-25D engine and is also small compared to p_{ull}. We note that since it is a function of the engine only, it is expected to be the same for SLS. (Estimation of the frictional pressure drop in tubes is carried out in Appendix.)

Thus, NPSP condition will hold for the whole LH2 volume of the rescaled rocket perhaps only with the exception of very thin layer near the interface of thickness <1.5cm and with temperature 23K≤T≤ 24K. This conclusion hold for higher values of the environment heat density flow so long as the near wall temperature is (much) smaller than 23.8K, which corresponds to the wall temperature for the critical value of the environmental heat flux $\dot{q}_{envir} = 950W/m^2$.

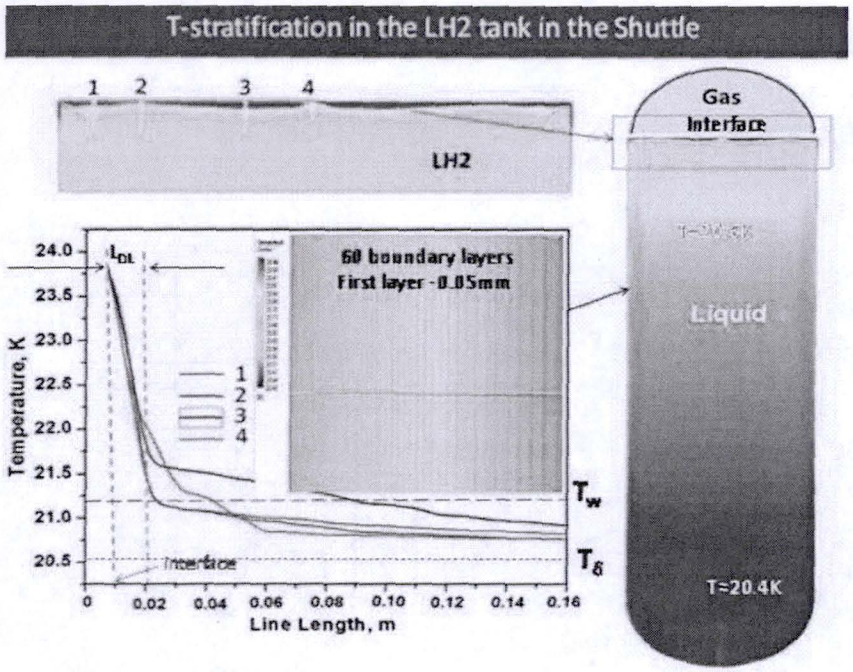

Fig.4-15. Temperature stratification in the LH2 tank in the Shuttle; t=500sec.

The temperature stratification pattern observed in the simulation (Fig. 4-15) corresponds well to the theoretical predictions. The warmest layer adjacent to the gas-liquid interface has temperature decreasing from T=23.8K to about T=21.2K, as predicted, over the legthscale of ~1cm, which corresponds to the thermodiffusion length scale l_{DL}=1.5cm calculated for t=500sec. The much wider weakly warmed layer at 20.4<T<21.2 is associated with the contribution of the outer turbulent sublayer of the natural convection. Based on the typical velocity in the ascending flow and its width (Fig. 4-11) the width of this weakly warmed layer can be estimated to be > 8m. To predict the temperature profile in this layer one has to acquire a better understanding of the transient characteristics of the turbulent flow pattern of ascending and

descending flows near the wall. However, for the scaling predictions for larger tanks it is important that the upper limit on the temperature in this layer is expected to stay at or below T=21.2K: this is due to even more developed turbulence in larger tanks, leading to stronger mixing and diffusion of the absorbed heat in larger bulk of liquid. This latter prediction was verified in a simulation of LH2 dynamics in a taller (by the factor 4/3) tank (Figure 4-16), which shows that the wall temperature T≈21K is independent of the size of the tank.

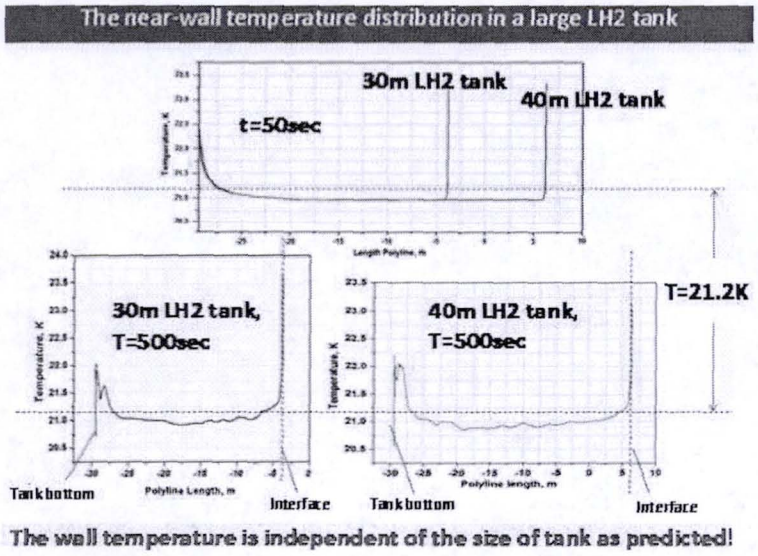

Fig.4-16. Temperature distribution along the wall in a large (40m high) LH2 tank vs. the Shuttle LH2 tank (30m high) ; t=50sec, 500sec.

Our predictions have been verified for the real Shuttle data (Fig. 4-17) for the temperature of the incoming fluid in the engine.

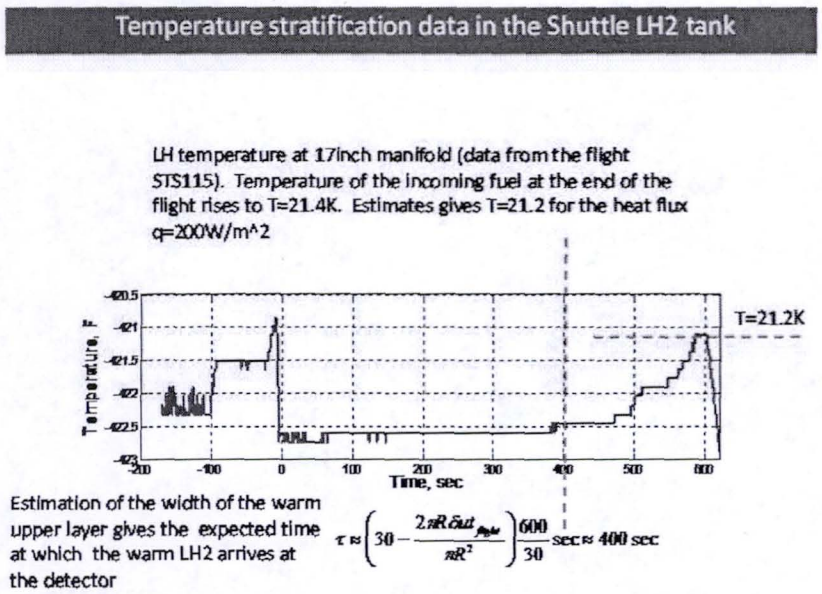

Fig.4-17 Temperature stratification data vs. predictions for the LH2 tank in the Shuttle.

One can see that both prediction of the near wall temperature T=21.2K and the width of the weakly warmed liquid layer >8m, correspond well to the data. In fact, the temperature of the incoming fluid rises to 21.4K in the end of the flight (the uppermost 1.5cm layer of the liquid at T=23.8K is shut-off), and taking the width of the warm layer 10m, we predict the beginning of the warm layer inflow at t=400sec.

In addition, we performed simulation and theoretical estimates of the stratification in Saturn LH2 tank, which we compared to the experimental data (Fig. 4-18), as published in [23].

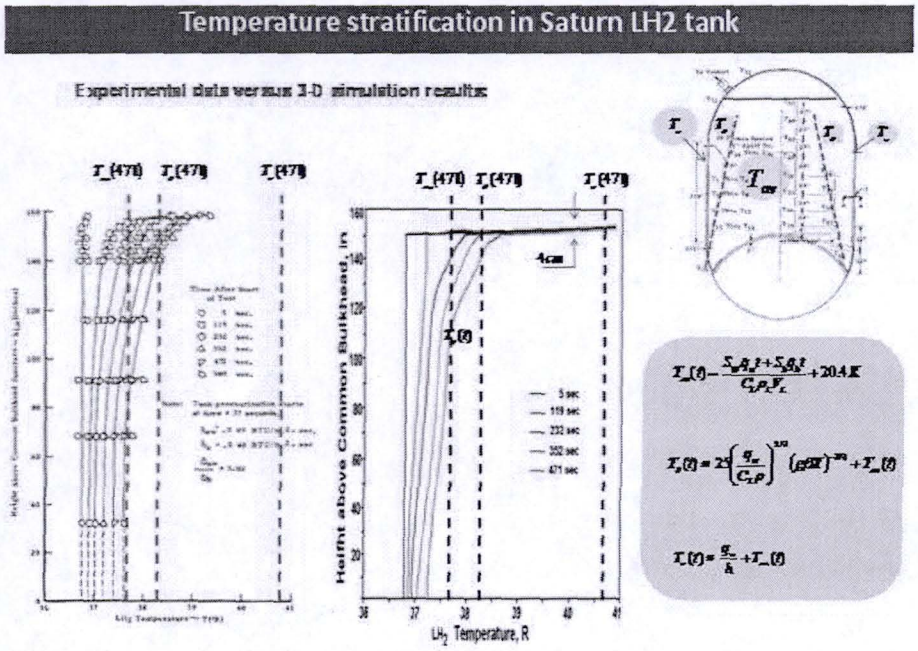

Fig.4-18 Temperature stratification data vs. predictions for the LH2 tank in Saturn.

To summarize the main results of our work on the temperature stratification:

1. Analysis of the turbulent natural convection correlation relations and the condensation-evaporation processes on the gas/liquid interface leads to a fairly accurate estimates of the liquid stratification pattern in LH2 tanks in the Space Shuttle and Saturn and predictions for larger tanks.
2. The main risk from the NPSP condition perspective is due to condensation-evaporation heating of a thin layer near the gas-liquid interface.
3. The temperature stratification is essentially invariant under the rescaling of the tank.
4. The interaction of the ascending natural convection flow with the descending forced convection flow leads to deviation from the theoretical predictions in the upper part of the tank.
5. However the interaction leads to development of a larger region of turbulence where the heat is efficiently diffused. As a consequence the main heating occurs still in the conductance (viscous) sublayer where the temperature is independent of the height of the tank
6. The temperature in the turbulent region is of no consequence from the NPSP condition standpoint. It is low in the Shuttle and is expected to be still lower in the larger tank (SLS) due to stronger turbulence. Numerical simulations of the LH2 dynamics in a larger tank support the validity of the theoretical arguments.

5. Effect of sloshing to LH2 tank

Intensive sloshing of cryogenic liquid (LH2) can occur after the start due to vibration of the rocket. Two main types of sloshing are shown in Fig.5-1: (i) the longitudinal sloshing waves excited by lateral forces and (ii) the axial sloshing (capillary waves) excited by parametrically forced oscillations.

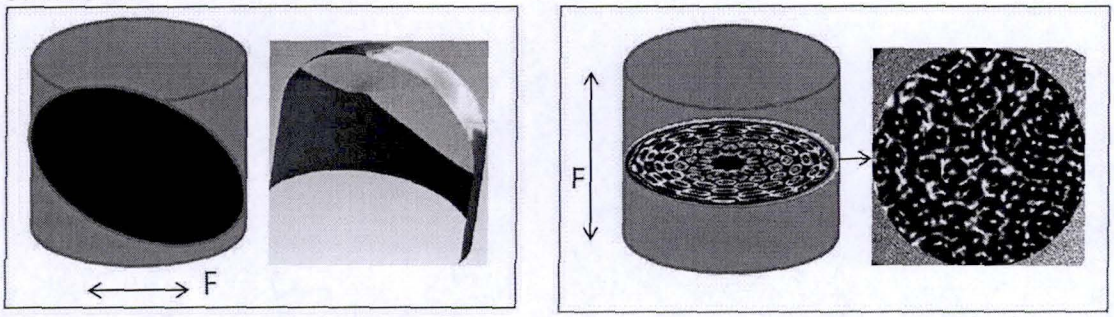

Fig.5-1 Two main types of sloshing: (i) Longitudinal sloshing waves excited by lateral forces (left); (ii) Axial sloshing (capillary waves) excited parametrically by axial vibrations (right)

5.1. Longitudinal sloshing waves

To understand main characteristics of the longitudinal sloshing waves (Fig. 5-2) consider a rigid tank with ideal inviscid liquid. We suppose that the surface waves are linear and the flow is potential

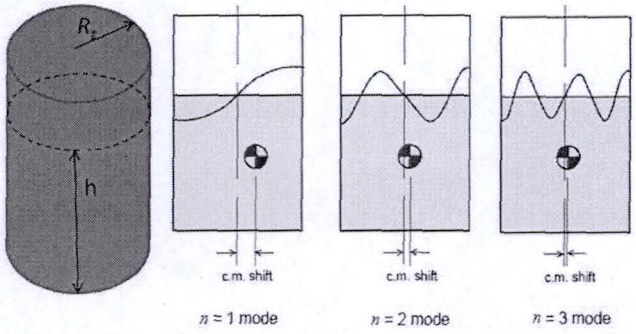

Fig.5-2 Main modes of longitudinal sloshing

Let us estimate the frequency of the surface oscillation assuming that the tank has cylindrical shape and that the motion is harmonic. In this case the velocity potential Φ satisfies Eq.(35)

$$\Delta\Phi = 0 \tag{34}$$

$$\frac{\partial^2\Phi}{\partial t^2} + g\frac{\partial\Phi}{\partial z} = 0 \text{ at at the free surface} z = h/2$$

$$\partial\Phi/\partial n = 0 \text{ at wall boundaries } z = -h/2 \text{and} r = R_t:$$

where h is height of the liquid level and n is a normal to the surface wall, g is a gravity. Analytical solution of the eigen-value problem is

$$\Phi_{mn}(r,z,\theta) = J_1(\lambda_{mn} r/a)\cos(m\theta)\frac{\cosh[\lambda_{mn}(z/a + h/2a)}{\cosh[\lambda_{mn} h/a]} \tag{35}$$

which represents eigen-functions and eigen-frequencies

$$\omega_{mn}^2 = \frac{g\lambda_{mn}}{a}\tanh(\lambda_{mn}h/a) \tag{36}$$

where r and θ are the radial and angular coordinates, a is the tank radius, and λ_{mn} (m,n=0,1,2..) is a root of the eigen value equation $dJ_1(\lambda_{mn}r/a)/dr = 0$ for $r = a$, ω is the angular frequency . The values of λ_{mn} for m =1 ($\cos\theta$) are $\lambda_{1n}=\xi_n$. Numerical values of ξ_n are: ξ_1 = 1.841, ξ_2=5.331, ξ_3 = 8.536. . . $\xi_{n+1} \rightarrow \xi_n + \pi$. For m = 1 the potential varies in the angular coordinate as $\cos\theta$, the wave is "up" over half the circumference and "down" over the other half.

Eigen-frequency of flexural sloshing oscillations is a function of the radius, gravity acceleration g, height of the tank h and values λ_{mn}. For the first nonsymmetrical mode (m=n=1) such frequency is presented as a function of tank radius in Figure 5-3 (left) and the oscillations as a function (a,h) is presented in Fig.5-3(right). It can be seen that for radius R_t=4.2m the period of the longitudinal antisymmetric sloshing wave is about T_{osc}=3 sec.

It should be noted that formula (36) doesn't contain density of the liquid, therefore the eigen-frequencies will be the same for liquid oxygen tank of the same radius.

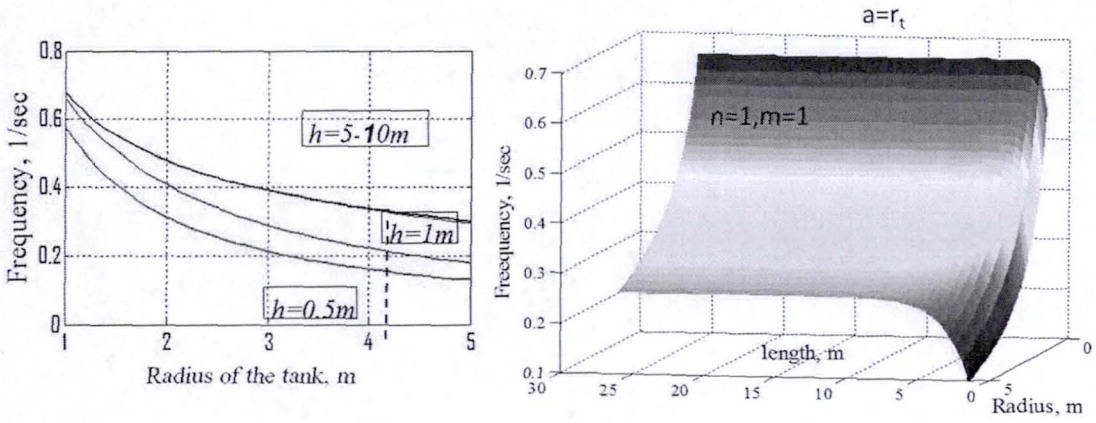

Fig.5-3. Frequencies of flexural mode oscillations for different tank radios and height

The longitudinal sloshing is responsible for three main effects: (i) sliding of cold liquid along the hot wall; (ii) growth of the area of the liquid surface; and (iii) mixing of the warm surface layer with the underlying cold layer.

(i) At the start of flight the motion of the rocket can induce an longitudinal sloshing wave with an amplitude A_{wave} and period T_{osc}.The cold liquid in contact with hot tank wall will heat up and evaporate. An upper bound on the evaporated mass can be estimated form the following condition: the heat accumulated in the wall is spent to heat the liquid and the vapor and to the evaporation, $Q_{wall} = Q_{vapor.}$:

$$Q_{wall} = \rho_w d_w \pi R_t \int_{0=\text{interface}}^{A_{wave}} C_w(T_{wall}(y))(T_{wall}(y)-T_s)dy \approx \bar{C}_w \rho_w d_w \pi R_t A_{wave}(\bar{T}_{wall}-T_s),$$
$$Q_{evap} = C_L M_L(T_s - T_L) + q_L M_L + C_g M_g(T_{g,evap} - T_s),\ M_g = M_L. \tag{37}$$

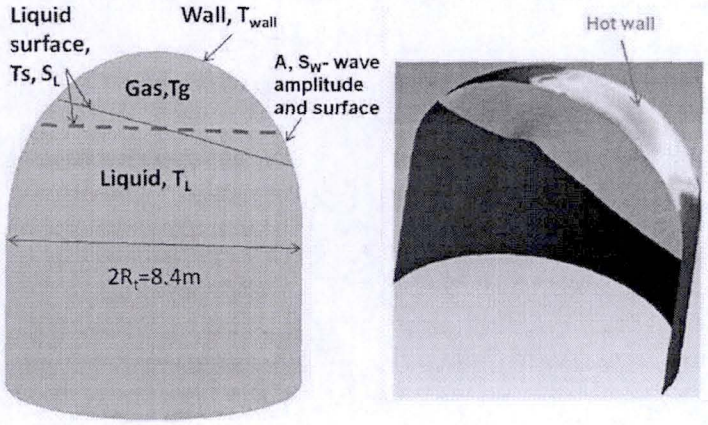

Fig.5-4. Sloshing brings cold liquid in contact with the hot tank wall

where we used the fact that the thermodiffusion length in AL 2195 $L_D(T_{osc}) \approx 7$mm is larger than the wall width $d_{wall} \approx 5$ mm. It follows from Eq. (37) that the maximum mass and volume of evaporated vapor during $t=T_{osc}$ are

$$M_{evap} \approx \frac{\pi R_t A_{wave} C_w d_w \rho_w (T_{wall} - T_s)}{q_L + C_g (T_s - T_L) + C_g M_g (T_{g,evap} - T_s)},$$

$$V_{eavp} = \frac{R_{H2} M_{evap} T_{evap}}{p_{tank}}, V_{eavp} = 0.2m^3 \left(\frac{\mathrm{A_{wave}}}{5\mathrm{cm}} \right) \text{ for } 20\mathrm{K} \le T_{evap} \le 50\mathrm{K}. \quad (38)$$

The pressure jump is calculated using the heat balance equation as follows:

$$dE = -pdV + dQ_W \Rightarrow \frac{V\Delta p}{\gamma - 1} = -\frac{\gamma p \Delta V}{\gamma - 1} + M_{evap} C_p T_{gas}, \quad \Delta V = \alpha \Delta p,$$

$\alpha = 0.3 \frac{m^3}{psi}$ - expansion coeffecient of the LH2 thank

$$\Delta p = \frac{M_{evap} R_{gas} T_{gas}}{V_{ullage,0} + \alpha \gamma p_{ullage}}, \quad (39)$$

$\Delta p < 0.027 atm$ for $\mathrm{A_{evap}} \le 15cm, V_{ullage} = 27m^3, \overline{T}_g \approx 100K$

$\Delta p_{\max} = 0.25 atm$ for max sloshing amplitude $\mathrm{A_{evap}} = 1.4m$

We see that for the *highly improbable hazardous event* when the amplitude of longitudinal sloshing oscillation at the moment of the engine start (t = - 6sec) equals its maximum value A_{wave}=1.4m the maximum volumes of evaporated vapor and the pressure jump can reach $V_{evap} = 5.6m^3$ and $\Delta p \approx 0.25$ atm for T_{osc}=3sec.

After the start (t > 0) the stationary longitudinal sloshing waves accelerate condensation by (ii) increasing the area of the liquid surface (minor effect); (iii) mixing the heated surface liquid layer with adjacent cold LH2 with $T=T_L$ (major effect). As a consequence, the thickness of the heated surface layer decreases but the interface temperature does not change, determined by

the partial GOx pressure: T =$T_s(p_{GOx})$ =23.8K. The condensation flow rate at the liquid-gas interface is limited by the heat balance between the hot gas T_g near the surface and the liquid surface with T=T_s:

$$j_{cond}(t)=\left[K_L\frac{T_s-T_L}{L_L(t)}-K_g\frac{T_g-T_s}{L_g(t)}\right]\frac{1}{q_L+C_{H2}\left(T_g-T_s\right)}. \tag{40}$$

The maximum value of the condensed mass M_{cond} induced by the sloshing can be estimated assuming complete mixing of the surface layers of cold and warm liquid over each period of oscillation. Due to such intensive mixing the width of the heated liquid layer over a fraction S_L^* of the surface area will be very small at end of each oscillation, $L_L \to 0$ (Fig. 5-5).

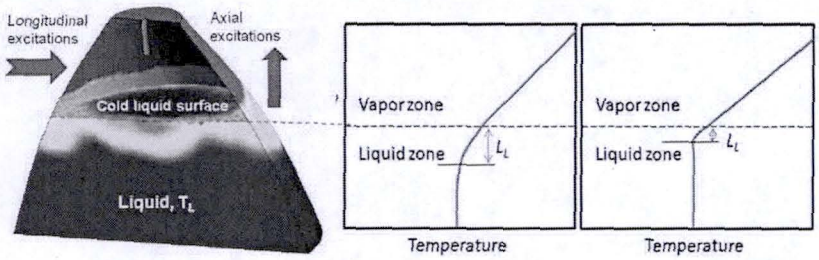

Fig. 5-5. Sketch of the temperature distribution before and during the sloshing

In this case the first term in the right part of Eq. (40) is much larger than the second. Therefore, the mass condensed over one period can be estimated as

$$M_{cond}(T_{osc})=\int_o^{T_{osc}} S_L^* J_{cond}(t_1)dt_1 \approx S_L^*\left(T_s-T_L\right)\frac{\sqrt{K_L C_L \rho_L}}{q_L+C_{H2}\left(T_g-T_s\right)}\left(\sqrt{\frac{4T_{osc}}{\pi}}\right), \tag{41}$$

The total condensed mass induced by the longitudinal waves over the time of t is given by

$$M_{cond}^{slosh}(t)=M_{cond}(T_{osc})\frac{\Delta S_L+S_L}{S_L}\left(\frac{t}{T_{osc}}\right),\ \frac{\Delta S_L+S_L}{S_L}=\frac{\sqrt{R_t^2+A_{wave}^2}}{R_t}. \tag{42}$$

The total condensation flux is equal to

$$\max J_{cond}^{slosh}=\frac{\max M_{cond}^{slosh}(t)}{t}=0.023\frac{kg}{\sec} \tag{43}$$

$$T_s(p_{GH2})=23.8K,\ 24K<T_g\le 50K \text{ near the interface}$$

It should be compared to the much larger the flux of the injected hot GH2: $J_{GH2}=0.35\frac{lb}{\sec}=0.476\frac{kg}{\sec}\times\left[N_{nozzle}/3\right]$, N_{nozzle} – nozzle nozzle in SLS

Thus, the longitudinal sloshing waves cannot appreciably change the ullage pressure.

Effect of sloshing is expected to be even smaller for the SLS since the flow rate of injected hot GH2 will increase with larger nozzle number. However, SLS vehicle has higher thrust and one can expect stronger vibrations due to adding one or two RS-25 engines.

Conclusion about the acceleration of condensation by the longitudinal sloshing is confirmed by experimental data [23] presented in Fig. 5-6. The pressure in the ullage space increases from 15psi to p_0=35 psi due to hydrogen pressurization with temperature 40K during 15sec.

After 50 sec lateral vibrations are observed with frequencies f=0.95Hz (non-resonance influence) and 0.74Hz (resonant vibrations stimulate intensive sloshing). The ullage pressure slowly decreases in the case of the vibrations with f=0.95Hz and sharply drops in the case of the resonant vibrations with f=0.74Hz.

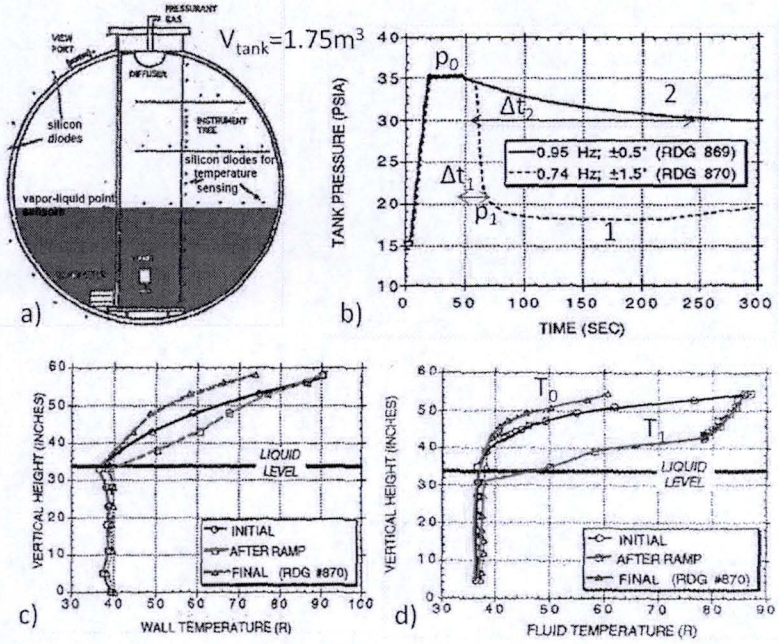

Fig. 5-6. Sketch of the tank and the internal instrumentation (a), pressure response for the sloshing test (b), wall temperature (c) and ullage space temperature (d).

The condensation flow density rate can be estimated from the equations

$$\rho(t)V = \rho_0 V - j_{cond} S \cdot t,\ p_0 V = \rho_0 V R_{H2} T_0,$$
$$p_1 V = \left(\rho_0 V - j_{cond} S \cdot t_1\right) R_{H2} T_1\ (\mathrm{R}_{H2} = 4124 \tfrac{J}{kgK}), \tag{44}$$
$$j_{cond} = \left(p_0 \frac{T_1}{T_0} - p_1 \right) \frac{V}{R_{H2} T_1 S \cdot t_1}$$

It follows from Eq. (44)

$$j_{cond,1} \simeq 4.5 \cdot 10^{-3} \frac{kg}{m^2 \sec} \text{ for resonance (f=0.74Hz)}$$
$$\text{for } p_0\text{=35psi, } p_1\text{=20psi, } \Delta t\text{=20sec, } V_{ullage}\text{=0.35}V_{tank}\text{=0.63m}^3\text{, S=1.6m}^2\text{,} \tag{45}$$
$$j_{cond,2} \simeq 3.3 \cdot 10^{-4} \frac{kg}{m^2 \sec} \text{ for non-resonance (f=095Hz)}$$

We use the data of Eq. (45) for estimation of the condensation rate for LH2 tank

$$J_{cond} \simeq j_{cond,1} \cdot S_{tank} \left(T_{osc} f_1\right)^{1/2} \simeq 0.16 \frac{kg}{\sec} \text{ for resonance influence } (f_1\text{=0.74Hz})$$
$$j_{cond} \simeq j_{cond,1} \cdot S_{\text{tank}} \left(T_{osc} f_2\right)^{1/2} \simeq 0.014 \frac{kg}{\sec} \text{ for non-resonance influence } (f_2\text{=0.95Hz}) \tag{46}$$

The foregoing estimation $J_{cond}^{slosh} \simeq 0.025 \frac{kg}{\sec}$ for the condensation rate for intensive sloshing given by Eq. (42) agrees with the data of Eq. (46).

5.2. Axially excited sloshing: generation of droplets

The thrust oscillations initiate axial excitation and lead to Faraday instability of the liquid surface. Intensive oscillations of these modes can result in the liquid level discontinuity and generation of the liquid droplets under the liquid-gas interface. This process will change heat balance on the interface. Evaporation of the cold liquid droplets into the hot ullage gas can increase the ullage pressure during the beginning stage of the flight. At the same time enlarging the cold surface can accelerate condensation. Since the rate of evaporation of liquid hydrogen depends on partial pressure of gaseous H2, in the case where He is used as the pressurization gas we expect enhanced evaporation and consecutive increase in a ullage gas pressure. For gaseous Hydrogen pressurization these droplets will enhance the condensation rate.

Theoretical treatment of the droplet ejection is given in many articles. Linear theory is described by dispersion relation obtained from equation (34) with the same boundary conditions, where for small wavelength capillary waves we should take into account surface tension σ :

$$\omega^2 = \left(gk + \frac{\sigma}{\rho} k^3 \right) \tanh(kh) \tag{47}$$

where k=2π/λ, λ as the wavelength, is the wave number and ρ is the liquid density. At small k<<1 this equation is identical to equation (36):

$$\omega_{mn}^2 = \frac{g\lambda_{mn}}{a} \tanh(\lambda_{mn} h / a) \tag{48}$$

The nonlinear dynamics of the droplet formation and ejection is extremely complicated and strongly depends on the rocket vibrations spectrum. Here we carry out a simplified analysis of this dynamics. The typical diameter of ejected droplets is about [24,25]

$$d_{drop} \simeq (\sigma_L / \rho_L)^{1/3} \omega^{-2/3}, \quad \omega = 2\pi f \tag{49}$$

where ρ_L=70kg/m^3 and σ_L=0.0017N/m are liquid density and surface tension, ω is vibration frequency ($\omega=2\pi f_{vibr}$). Characteristic values of d_{drop} are shown in Fig.5-7 (left).

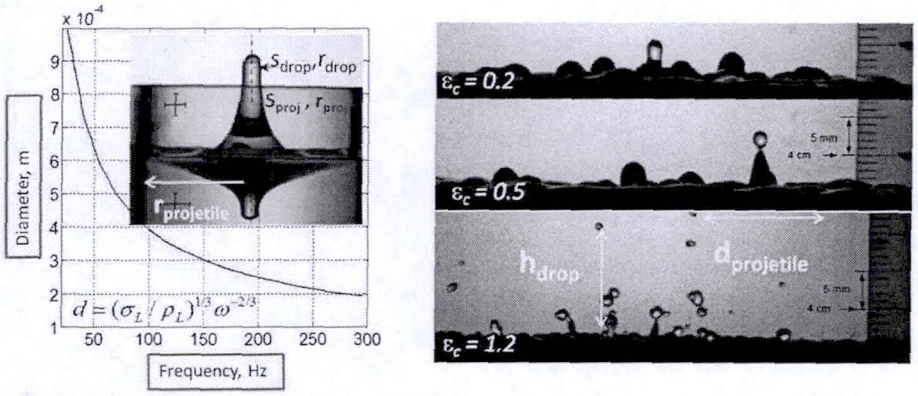

Fig.5-7. The typical diameter of ejected droplets as a function of the thrust oscillation frequency (left) ; generation of droplets under action of supercritical vibration acceleration ε_d>0 [26].

Each projectile area of diameter $d_{proj} \approx 5d_{drop}$ ejects the droplet with a rate given by [24,25]

$$dn/dt \equiv \dot{n} = 0.04\varepsilon_{,l}^{2.8}\omega\,[s^{-1}], \varepsilon_d = (a_{vibr} - a_d)/a_d,$$
$$a_d = 0.26(\sigma/\rho)^{1/3}\omega^{4/3} \tag{50}$$

Here a, ω are vibration acceleration and frequency, a_d is the critical driving acceleration for the onset of droplet ejection. The droplet ejection occurs when the frequency and amplitude of vibration A_{vibr} satisfy the condition:

$$a_{vibr} = A_{vibr}\omega^2 > a_d \text{ or } A_{vibr} > A_c = 0.1mm(100Hz/f_{vibr})^{2/3},$$
$$A_c = 0.25mm \text{ for } f = 25Hz, A_c = 65\mu m \text{ for } f = 200Hz \tag{51}$$

Sufficiently strong vibrations can occur only after the start. At this point the thermo-diffusion length in the liquid has increased to the value of L_D (100sec)≈7mm during the prepress (t ≈ 100sec). This value is much greater than the typical drop diameters: $L_D \simeq 7mm >> d_{drop}$ for $f > 50Hz$. It follows that the inner temperature of generated droplets T_{drop} is close to the surface temperature of the liquid $T_s(p_{GH2})$. Therefore, the liquid mass evaporated due to the vibration is very small. Indeed, the mass evaporated from the surface of single droplet s_{drop} during the droplet life-time t_{drlife} can be estimated as

$$m_{evap}(t_{drlife}) = s_{drop}\int_{t_{press}}^{t_{press}+t_{drlife}} j_{evap}(t)dt \le \frac{J_{cond}(t_{press})s_{drop}}{S_L}t_{drlife}, t_{drlife} = \sqrt{\frac{2h_{drop}}{g}},$$
$$J_{evap}(t) = S_L\frac{\left(T_g - T_s(p_{GH2})\right)\sqrt{K_gC_g\rho_g} - \left(T_s(p_{GH2}) - T_{drop}\right)\sqrt{K_LC_L\rho_L}}{\left(q_L + C_g\left(T_g - T_L\right)\right)\sqrt{\pi t}}, \tag{52}$$

where h_{drop} is the maximum height an ejected droplet rises above the surface (see Fig. 6-7). The total evaporated mass is given by

$$M_{evap} \le m_{evaop}(t_{drlife})\frac{dN_{drop}^{total}}{dt}t = m_{cond}(t_{drop})\frac{S_L\dot{n}_{drop}}{s_{proj}}t,$$
$$where \frac{dN_{drop}^{total}}{dt} = \frac{S_L\dot{n}_{drop}}{s_{proj}}, \dot{n}_{drop} - \frac{dn_{drop}}{dt} \tag{53}$$

Here dN_{drop}^{total}/dt is total number of droplets ejected over unit time from the liquid surface S_L. Taking into account Eq. (52) and condition $d_{proj} \approx 5d_{drop}, s_{drop}/s_{proj} = 4/25$ we conclude from Eq.(53) that the total evaporation mass is a negligible quantity

$$M_{evap} \le J_{evap}(t_{press})t_{drlife}\frac{4\dot{n}_{drop}t}{25} \le \frac{4J_{evap}(T_{prepress})t}{25}, \dot{n}_{drop} \le \frac{1}{T_{drlife}},$$
$$J_{evap} \le M_{evap}/t = 0.16J_{evap}(T_{prepress}) \le 0.8g/\sec \tag{54}$$

In the estimation we used the results of calculation presented in Sec.2 (see Fig. 2-4) $J_{evap}(T_{prepress}) \le 5g/\sec$.

An appreciable effect can occur only as a result of combined action of intensive longitudinal and axial sloshing vibrations (Fig. 5-5, left)). The maximum value of the condensed mass

induced by sloshing waves can be estimated assuming intensive mixing of surface layers of cold and warm liquid during each period. Due to such mixing the thickness of some area of the heated surface layer S_L^* will very small at end of each oscillation, $L_L \to 0$ (Fig. 5-5). Droplets generated by the axial sloshing will have T near $T_{L,}$, except for a very thin surface layer $L_L \to 0$ near the surface having $T=T_s(p_{GH2})$. In this case the maximum value of the condensed mass m_{cond} on the surface s_{drop} of a single droplet during the droplet life t_{drlife} can be estimated as

$$m_{cond}(t_{drlife}) = s_{drop}\frac{M_{cond}(t_{drlife})}{S_L} = \frac{s_{drop}\left(T_s(p_{GH2})-T_L\right)\sqrt{K_L C_L \rho_L}}{q_L + C_{H2}\left(T_g - T_s\right)}\sqrt{\frac{4t_{drlife}}{\pi}},\ t_{drlife} \approx \sqrt{\frac{2h_{drop}}{g}} \tag{55}$$

and the total condensation flux from all the ejected droplets is

$$J_{cond}^{total} = m(t_{drlife})\frac{dN_{drop}^{total}}{dt} = \left(\frac{4}{25}\right)\frac{S_L^* m(t_{drlife})\dot{n}_{drop}}{s_{drop}},\ \dot{n}_{drop} \le \frac{1}{t_{drlife}} \text{ for } A_{vibr} > Ac,$$

$$J_{cond}^{total} \le \frac{8S_L^*\left(T_s(p_{vapor})-T_L\right)\sqrt{K_L C_L \rho_L}}{25\left[q_L + C_{vapor,p}\left(T_g - T_s\right)\right]}\sqrt{\frac{1}{\pi t_{drlife}}},\quad t_{drlife} = \sqrt{\frac{2h_{drop}}{g}}, \tag{56}$$

Using $S_L^* \approx S_L/3$ and $t_{drlife} \approx \sqrt{2h_{drop}/g} \approx 0.02\,\text{sec}$ we obtain from Eq.(56) that the total mass flow rate of condensed vapor on all ejected droplets is about $J_{drop}^{total} < 0.09 kg/\text{sec}$. We notice that the mass flow rate of injected hot GH2 is much more: $J_{GH2} = 0.35\frac{lb}{\text{sec}} = 0.476\frac{kg}{\text{sec}} \times \left[N_{nozzle}/3\right]$.

As a result of the condensation the ejected droplets will be heated and falling back into the liquid will increase the temperature of the liquid surface layer. The width of the heated surface liquid layer can be found from the heat balance equation

$$J_{drop}^{total}\left[q_L + C_{GH2}\left(T_g - T_s\right)\right]\cdot t = C_L\rho_L\left(T_s - T_L\right)S_L \cdot l_{heated}^{liquid},$$

$$l_{heated}^{liquid}(t) = \frac{S_L^*}{S_L}\left(\frac{8L_D(t)}{25\pi}\right)\left(t\cdot t_{drlife}\right)^{1/2}\dot{n}_{drop},\ t_{drlife} = \sqrt{\frac{2h_{drop}}{g}}, \tag{57}$$

$$l_{heated}^{liquid}(t_{flight}) \le 5L_D(t_{flight}) = 7.5cm \text{ for } \dot{n}_{drop} \le 1/t_{drlife},\ t_{drlife} < 0.02\,\text{sec}$$

Thus, *combined action of longitudinal and axial sloshing vibrations can lead to formation of relatively thick hazard surface layer of heated liquid with temperature T≈23.8K, thickness L≈7.5cm, volume* , $V_{heat} = S_{tank}L_{heated}^{total}/2 = 2m^3$ *and mass* $M_{heat} = V_{heat}\rho_L = 140kg$. Total mass of LH2 in the tank is 105,000kg

SLS vehicle has higher thrust and expected vibrations due to adding one or two RS-25 engines. At the same time the mass flow rate of injected hot GH2 increases with the engine number. All the effects under consideration are taking place in a narrow layer adjacent to the interface. Therefore the influence of these effects on both the mass and the heat balance in the tank will not be critical. However, the effect of heating of relatively thin layer to T≈23.8K can arise in LH2 SLS tank because possible intensive longitudinal and axial sloshing vibrations .

6 Conclusion

We performed theoretical investigation of main physics processes in LH2 tank during pre-starting prepress and rocket flight that can lead to possible hazards in the case of rescaling of main parameters of Shuttle with regard to proposed LH2 tank designs for SLS with 5 engines (the situation with 4 engines is less critical). Our investigations based both on theoretical analysis and on MNM and 3D simulations allow us to make the following conclusions

1. Hazard analysis for LH2 ET shows that the pressure control bandwidth remains almost the same for the SLS.

2. The MNM can reproduce accurately the pressure during pre-press and blow down.

3. For the GHe and GH2 flow rates and the initial ullage volume rescaled by 5/3 for the SLS LH2 ET, no new hazards are found for the tank performance; the temperature stratification is more pronounced in the rescaled SLS tank.

4. The bubble formation at the tank wall does not scale with the tank length but it's effect is still relatively small and will not considerably affect the performance.

5. Effect of condensation and evaporation are also relatively small.

6. The temperature stratification of the liquid reveals a structure consisting of three layers:

(i) The upper hearted layer of thickness less than 0.6in=1.5cm at the end of the flight and with temperature 21.2K<T< 23.8K;

(ii) The intermediate warm layer of width <8in=20cm at the end of the flight and with temperature 20.6K<T < 21.2K;

(iii) The lower warm layer with 20.4K<T<21.6K of width ~10m at the end of the flight.

In (i), both the temperature and the width of this layer are invariant under the 5/3 rescaling of the tank length. In (ii-iii), the sub-layer is formed due to the rising warm liquid flow with T=21.2K forming in a thin boundary layer near the wall and accumulating near the interface. These sub-layers will increase by a factor of 5/3 under the scaling but its temperature will be T< 21.2K.

7. The NPSP condition holds for the rescaled rocket with the exception of the upper hearted layer of thickness less than 0.6in=1.5cm . Maximum mass and energy of such overheated liquid with T=23.8 is less than 30kg and 2.5×10^5 J. Total LH2 mass and energy in the filled tank are 105270kg and 3.4×10^8 J. Therefore, it does not play the role in the ullage temperature stratification and pressure dynamics.

8. Intensive longitudinal sloshing waves induced by the laterally excited rocket vibration change weakly the temperature liquid and ullage stratification and the ullage pressure during the flight. Maximum rate of condensation flow arising due to the strong mixing of the warm surface liquid layer with the cold deep layers is limited by value of $J_{cond}^{slosh} = 0.023 \frac{kg}{\sec}$. The mass flow rate of injected hot gas (GH2 or GOx) is much more $J_{GOx}(t) = 0.476 \frac{kg}{\sec} \times (n_{nozzle} / 3)$, n_{nozzle} is nozzle number in the SLS.

9. The vertical vibrations with the amplitude A_{vibr} and the frequency f_{vibr} such as $A_{vibr} > A_c = 0.1mm(100Hz / f_{vibr})^{2/3}$ induce generation of the warm droplets under the liquid-gas interface. Effect of axially excited vibration sloshing on LOx tank is extremely small as the temperature of generated warm droplets is very close to the interface temperature and condensation is depressed.

10. Combined action of intensive longitudinal and axial sloshing vibrations can induce relatively great condensation and formation of relatively thick hazard surface layer of heated liquid with temperature $T=T_s(p_{GOx})$. The rate of the condensation can reach $J_{drop}^{total} = 0.09 kg / \sec$ and thickness, volume, and mass of surface heated layer can reach L_L=7.5cm, V=4m^3, and 280kg. Total LH2 mass and energy in the filled tank are 105270kg.

11. The longitudinal and axial sloshing waves cannot appreciably change the ullage pressure. Effect of sloshing is expected to be even smaller for the SLS since the flow rate of injected hot GH2 will increase with larger nozzle number. However, SLS vehicle has higher thrust and one can expect stronger vibrations due to adding one or two RS-25 engines. Combined action of intensive longitudinal and axial sloshing vibrations can lead to formation of relatively thick hazard surface layer of heated liquid with temperature T≈23.8K, thickness L≈7.5cm and volume (mass) V=4m^3.(280kg).

12. SLS vehicle has higher thrust and expected vibrations due to adding one or two RS-25 engines. While the mass flow rate of injected hot gases increases with the engine number. All the effects under consideration are taking place in a narrow layer adjacent to the interface and

the influence of these effects on both the mass and the heat balance in the tank will not be critical. However, the effect of heating of relatively thin layer to T≈23.8K can arise in LH2 SLS tank because of possible intensive longitudinal and axial sloshing vibrations.

7 Appendix

The pressure drop in a tube with turbulent flow due to the wall friction can be estimated as

$$\Delta p_{fric} = 0.02\rho_L u^2 \left(\frac{l_{tube}}{r_{tube}}\right)(\mathrm{Re})^{-1/4}, \mathrm{Re} = \frac{u r_{tube}}{\mu L}, u = \frac{J_L}{\pi r_{tube}^2 \rho_L}, \mathrm{Re} = \frac{J_L}{\pi r_{tube} \mu_L},$$

$$\Delta p_{fric} = \frac{0.02}{\rho_L}\left(\frac{l_{tube}}{r_{tube}}\right)\left(\frac{J_L}{\pi r_{tube}^2}\right)^2\left(\frac{J_L}{\pi r_{tube}\mu_L}\right)^{-1/4} = \Delta p_{fric,0}\left(\frac{l_{tube}}{l_{tube,0}}\right)\left(\frac{J_L}{J_{L0}}\right)^{7/4}\left(\frac{r_{tube}}{r_{tube},0}\right)^{-19/4} \quad (58)$$

$$\mathrm{Re} > 4\times 10^7 \text{ for } J_L > 200 kg/\sec \text{ and } r_{tube} > 0.2m \text{ (turbulent condition)}$$

Requirement for the feedline follows form Eq.(58)

$$p_{fric} < 0.1 atm \text{ for J=200kg/sec (3engines) at tube radius } r_{tube}\text{>7.5cm(3in)}$$
$$\text{or for J=333kg/sec (5engines) at tube radius } r_{tube}\text{>9cm(3.5in)} \quad (59)$$

Thus, in order to keep the same pressure drop in the feedlines in scalable SLS LH2 tank it is necessary to increase the tube radius on 20% or 10% for nozzle number N_{nozzle}=5(4):

$$\left(\frac{r_{tube}}{r_{tube},0}\right) = \left(\frac{l_{tube}}{l_{tube,0}}\right)^{4/19}\left(\frac{J_L}{J_{L0}}\right)^{7/19} = \left(\frac{l_{tube}}{l_{tube,0}}\right)^{4/19}\left(\frac{N_{nozzle}}{3}\right)^{7/19},$$
$$\left(\frac{r_{tube}}{r_{tube},0}\right) = 1.2(1.1) \text{ for } n_{nozzle} = 5(4) \text{ and } l_{tube} = l_{tube,0}. \quad (60)$$

References

[1] "STS-115 ET-MPS Predicted Performance", Marshall Space Flight NASA Center Report, 4160/P-06-4011, August, 2006.

[2] "Space Shuttle External Tank Drawing", Propulsion Data Thermo-Book, No. 80900200103, Lookheed Martin, 2005.

[3] L. Norquist, "External tank for the Space Shuttle Main Propulsion System", J. Spacecraft, 14, 358 (1977); G. M. Mactin, "A stratification prediction technique *for* cryogenic hydrogen and oxygen tanks under high-g conditions", October 1971, Summary Report, ASD-ASTN-1414, NASA MSF Center.

[4] P. N. Estey, D. H. Lewis Jr. and M. Connor, "*Prediction of a Propellant Tank Pressure History Using State Space Methods*", J. of Spacecraft and Rockets, 20, pp. 49-54 (1983).

[5] Schallhorn, P., Campbell, D. M., Chase, S., Puquero, J., Fontenberry, C., Li, X., Grob, L., "Upper Stage Tank Thermodynamic Modeling Using SINDA/FLUINT", AIAA-2006-5051, 44rd

AIAA/ASME/SAE/ ASEE Joint Propulsion Conference and Exhibit, Sacramento, CA, July 9-12, 2006.

[6] B. T. Burchett, "Simulink Model of the Ares I Upper Stage Main Propulsion System", AIAA (2008).

[7]R. C. Hendricks, A. K. Baron, and I. C. Peller, "GASP-A Computer Code for Calculating the Thermodynamic and Transport Properties for ten Fluids" TN D-7808, Feb: 1975, NASA.

[8] A. Clark, IAA/ASME/SAE/ASEE Joint Propulsion Conference and Exhibit, 2004, unpublished paper, No. AIAA 2004-4088.

[9] V.V. Osipov, C.B. Muratov, "*Dynamic condensation blocking in cryogenic refueling*", Applied Physics Letters, 93, 224105 (2008).

[10] "Experimental and analytical investigation of interfacial heat and mass transfer in a pressurized tank containing liquid hydrogen", *by WiZZium A. OZsen, Lewis Research Center Cleveland, Ohio,* NASA TECHNICAL NOTE.-D-3219, March ,1966.

[11]. A. N. Khalifa, "Natural convective heat transfer coefficient - a review I. Isolated vertical and horizontal surfaces", Energy Conversion and Management 42 (2001) 491-504

[12] E. R. G. Eckert and T. W. Jackson, Analysis of Free-Convection Boundary Layer on Flat Plate, National Advisory Committee for Aeronautics technical memorandum No. 2207, Washington, September 1950

[13] W. K. George and S. P. Capp, A theory for natural convection turbulent boundary layers next to heated vertical surfaces, Int. J. Heat Mass Transfer 22, p.813 (1979)

[14] T. Tsuji and Y. Nagano, "Characteristics of a Turbulent Natural Convection Boundary Layer along a Vertical Flat Plate", Int.J Heat Mass Transfer, Vol. 31, No 8, pp. 1723-1734 (1988).

[15] T. Tsuji and Y. Nagano, "Turbulence Measurements in a Natural Convection Boundary Layer along a Vertical Flat Plate", Int.J Heat Mass Transfer, Vol. 31, No 10, pp. 2101-2111 (1988).

[16] A. J. Wells and M. G. Worster, A geophysical-scale model of vertical natural convection boundary layers, J. Fluid Mech. (2008), vol. 609, pp. 111–137

[17] Schmidt, F. W., Henderson, R. E., and Wolgemuth, C. H., Introduction to Thermal Sciences, J. Wiley & Sons, Second Ed., 1993.

[18] J. W. Tatom, W. H. Brown, L. H. Knight and E. F. Coxe, Analysis of Thermal Stratification of Liquid Hydrogen in Rocket Propellant Tanks," Presented at Cryogenic Engineering Conference, August, 1963.

[19] F. H. Morse, Turbulent Free Convection Over a Uniformly Heated Surface with Internal Heat Generation and a Non-Uniform Bulk Temperature, January, 1962, LMSC-FM-42.

[20] D. M. Tellep and E. Y. Harper, An Approximation of Propellant Stratification, Lockheed Missiles and Space Company, Note LMSC/80ZI44, October, 1962.

[21] R.W. Arnett and R.O. Voth, "A Computer Program for the Calculation of Thermal Stratification and Self- Pressurization in a Liquid Hydrogen Tank," NBS, NASA CR-2026,May 1972

[22] Schallhorn, P., Campbell, D. M., Chase, S., Puquero, J., Fontenberry, C., Li, X., Grob, L., "Upper Stage Tank Thermodynamic Modeling Using SINDA/FLUINT", AIAA-2006-5051, 44rd AIAA/ASME/SAE/ ASEE Joint Propulsion Conference and Exhibit, Sacramento, CA, July 9-12, 2006

[23] D. O. Barnett, T. W. Winstead and L. S. McReynolds, An Investigation of LH2 Stratification in a large Cylindrical Tank of the Saturn Configuration, NASA, MSFC.

[24] M. E. Moran, N B. McNelis, M. T. Kudlac M. S. Haberbusch and G. A. Satornino. Experimental Results of Hydrogen Slosh in a 62 Cubic Foot (1750 Liter) Tank. AIAA-94-3259 (1994).

[25] S. P. Das and E. J. Hopfinger. Parametrically forced gravity waves in a circular cylinder and finite-time singularity. J. Fluid Mech. 599, pp. 205–228 (2008).

[26] B. A. Puthenveettil and E. J. Hopfinger, "Evolution and breaking of parametrically forced capillary waves in a circular cylinder", J. Fluid Mech. 633 pp 355-379 (2009).